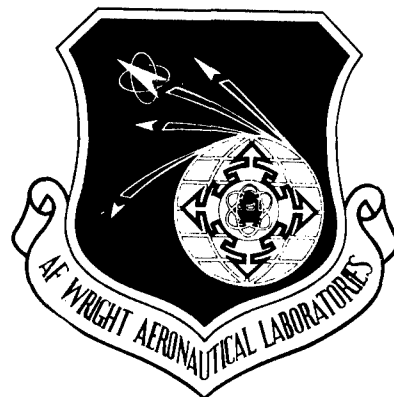


ADA 167981



MORPHOLOGY OF A PHASE SEPARATED AND A
MOLECULAR COMPOSITE 30%PBT/70%ABPBI POLYMER BLEND

W. W. Adams and J. F. O'Brien
Polymer Branch
Nonmetallic Materials Division

T. B. Haddock and S. J. Krause
Dept. of Mechanical and Aerospace Engineering
Arizona State University
Tempe, AZ 85287

P. G. Lenhart
Dept. of Physics
Vanderbilt University
Nashville, TN 37235

G. E. Price
University of Dayton Research Institute
Dayton, OH 45469

March 1986

Final Report for Period July 1982 - July 1985

Best Available Copy

Approved for Public Release; Distribution Unlimited

MATERIALS LABORATORY
AIR FORCE WRIGHT AERONAUTICAL LABORATORIES
AIR FORCE SYSTEMS COMMAND
WRIGHT-PATTERSON AFB, OH 45433

20040219265

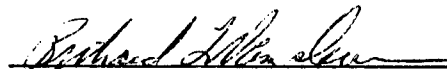
When Government drawings, specifications, or other data are used for any purpose other than in connection with a definitely related Government procurement operation, the United States Government thereby incurs no responsibility nor any obligation whatsoever; and the fact that the Government may have formulated, furnished, or in any way supplied the said drawings, specifications, or other data, is not to be regarded by implication or otherwise as in any manner licensing the holder or any other person or corporation, or conveying any rights or permission to manufacture use, or sell any patented invention that may in any way be related thereto.

This report has been reviewed by the Office of Public Affairs (ASD/PA) and is releasable to the National Technical Information Service (NTIS). At NTIS, it will be available to the general public, including foreign nationals.

This technical report has been reviewed and is approved for publication.



WALTER W. ADAMS
Project Scientist



RICHARD L. VAN DEUSEN
Chief, Polymer Branch

FOR THE COMMANDER



MERRILL L. MINGES, SES
Director
Nonmetallic Materials Division

"If your address has changed, if you wish to be removed from our mailing list, or if the addressee is no longer employed by your organization please notify AFWAL/MLBP, Wright-Patterson AFB OH 45433 to help us maintain a current mailing list."

Copies of this report should not be returned unless return is required by security considerations, contractual obligations, or notice on a specific document.

REPORT DOCUMENTATION PAGE

1a. REPORT SECURITY CLASSIFICATION Unclassified			1b. RESTRICTIVE MARKINGS									
2a. SECURITY CLASSIFICATION AUTHORITY			3. DISTRIBUTION/AVAILABILITY OF REPORT Approved for public release; distribution unlimited									
2b. DECLASSIFICATION/DOWNGRADING SCHEDULE												
4. PERFORMING ORGANIZATION REPORT NUMBER(S) AFWAL-TR-85-4108			5. MONITORING ORGANIZATION REPORT NUMBER(S)									
6a. NAME OF PERFORMING ORGANIZATION Air Force Wright Aeronautical Laboratories, Materials Lab.		6b. OFFICE SYMBOL (If applicable) AFWAL/MLBP	7a. NAME OF MONITORING ORGANIZATION									
6c. ADDRESS (City, State and ZIP Code) Wright-Patterson Air Force Base, Ohio 45433			7b. ADDRESS (City, State and ZIP Code)									
8a. NAME OF FUNDING/SPONSORING ORGANIZATION same as 6a.		8b. OFFICE SYMBOL (If applicable)	9. PROCUREMENT INSTRUMENT IDENTIFICATION NUMBER									
8c. ADDRESS (City, State and ZIP Code)			10. SOURCE OF FUNDING NOS.									
			<table border="1"> <tr> <th>PROGRAM ELEMENT NO.</th> <th>PROJECT NO.</th> <th>TASK NO.</th> <th>WORK UNIT NO.</th> </tr> <tr> <td>61102F</td> <td>2303</td> <td>Q3</td> <td>07</td> </tr> </table>		PROGRAM ELEMENT NO.	PROJECT NO.	TASK NO.	WORK UNIT NO.	61102F	2303	Q3	07
PROGRAM ELEMENT NO.	PROJECT NO.	TASK NO.	WORK UNIT NO.									
61102F	2303	Q3	07									
11. TITLE (Include Security Classification) Morphology of a Phase Separated and a (cont.)												
12. PERSONAL AUTHOR(S) W.W. Adams, J.F. O'Brien, T.B. Haddock, S.J. Krause, P. G. Lenhert, G. E. Price												
13a. TYPE OF REPORT Final		13b. TIME COVERED FROM <u>July 82</u> TO <u>Jul 85</u>	14. DATE OF REPORT (Yr., Mo., Day) March 1986	15. PAGE COUNT 83								
16. SUPPLEMENTARY NOTATION												
17. COSATI CODES			18. SUBJECT TERMS (Continue on reverse if necessary and identify by block number)									
FIELD	GROUP	SUB. GR.										
11	04		Molecular composites Electron microscopy									
07	04		Polymer blends Poly (p-phenylene benzobisthiazole)									
			X-ray diffraction Poly(2,5(6)benzimidazole)									
19. ABSTRACT (Continue on reverse if necessary and identify by block number) Scanning electron microscopy (SEM), transmission electron microscopy (TEM), analytical electron microscopy (AEM), and wide-angle x-ray diffraction (WAXD) were used to examine a polymeric blend of rigid-rod poly(p-phenylene benzobisthiazole), PBT, and semi-flexible coil poly(2,5(6)benzimidazole), ABPBI. When fiber and film were processed from a solution where the total polymer concentration of a 30% PBT/70% ABPBI blend was greater than a critical concentration, large-scale phase separation occurred and SEM images showed 0.1 micron to 4 micron ellipsoidal particles in a ductile matrix. TEM and AEM indicated these ellipsoids were chiefly composed of aggregates of well-oriented PBT crystallites with lateral dimensions of about 10 nm, while the matrix material was chiefly ABPBI. If the total polymer concentration of a 30% PBT/70% ABPBI blend was less than a critical concentration, the solution was optically homogeneous. During processing of the homogeneous solution into fiber and film, large-scale phase separation was inhibited by rapid coagulation in a water bath. Fiber and film processed in this manner did not show (cont.)												
20. DISTRIBUTION/AVAILABILITY OF ABSTRACT UNCLASSIFIED/UNLIMITED <input checked="" type="checkbox"/> SAME AS RPT. <input type="checkbox"/> DTIC USERS <input type="checkbox"/>			21. ABSTRACT SECURITY CLASSIFICATION Unclassified									
22a. NAME OF RESPONSIBLE INDIVIDUAL Dr. W. W. Adams			22b. TELEPHONE NUMBER (Include Area Code) (513) 255- 9148	22c. OFFICE SYMBOL AFWAL/MLBP								

11. TITLE (cont.)

Molecular Composite 30% PBT/70% ABPBI Polymer Blend

19. ABSTRACT (cont.)

any large-scale phase separation when examined by SEM and TEM. After heat treatment, this fiber and film were found to contain crystallites with lateral dimensions no larger than 3 nm, as determined by WAXD and TEM. Selected area electron diffraction and WAXD indicated crystallites of both PBT and ABPBI were present. In these samples the PBT homopolymer was dispersed in the matrix at the molecular level at a scale no larger than 3 nm. Any rod-rich phase separation was no larger than about 3 nm, resulting in a molecular composite. By processing from the homogeneous solution rather than from the phase-separated solution, orientation of both PBT and ABPBI in the blend was enhanced, as indicated by WAXD and TEM. In the molecular composite fiber, both the molecular-level dispersion and the enhanced orientation contributed to high values of mechanical properties.

FOREWORD

This report was prepared by the Polymer Branch, Nonmetallic Materials Division, and Vanderbilt University and Arizona State University (through Southeastern Center for Electrical Engineering Education) under Contract F49620-82-C-0035 to the Air Force Office of Scientific Research/AFSC. The work was initiated under Project No. 2303, "Research to Define the Structure Property Relationships," Task No. 2303Q3 Work Unit Directive 2303Q307, "Structure Resins." Dr. Thaddeus E. Helminiak served as the AFWAL/ML Work Unit Scientist. Co-authors were Dr. W. Wade Adams and Joseph F. O'Brien, Materials Laboratory (AFWAL/MLBP); Gary E. Price, University of Dayton Research Institute; Dr. Stephen J. Krause and Tim Haddock, Arizona State University; and Dr. P. Galen Lenhert, Vanderbilt University.

This report covers research conducted from July 1982 to July 1985.

TABLE OF CONTENTS

SECTION	PAGE
I INTRODUCTION	1
1. Concept of a Molecular Composite	1
2. Characterization Techniques	1
3. Previous Studies	3
a. PBT Fiber	3
b. ABPBI Fiber	5
c. Polymer Blend Fiber and Film	5
4. Objectives	10
II EXPERIMENTAL METHODS	12
1. Materials Processing	12
2. Sample Preparation	12
3. Equipment and Operation	15
a. Scanning Electron Microscopy	15
b. Wide Angle X-ray Diffraction	15
c. Transmission Electron Microscopy	15
d. Analytical Electron Microscopy	16
III RESULTS AND DISCUSSION	17
1. Scanning Electron Microscopy Imaging	17
2. Wide Angle X-ray Diffraction	19
a. PBT Fiber	23
b. ABPBI Fiber	25
c. 30% PBT/70% ABPBI $C > C_{cr}$ Fiber and Film	25
d. 30% PBT/70% ABPBI $C < C_{cr}$ Fiber and Film	27

TABLE OF CONTENTS (Concluded)

SECTION	PAGE
3. Transmission Electron Microscopy Imaging and Diffraction	31
a. PBT Fiber	36
b. ABPBI Fiber	37
c. 30% PBT/70% ABPBI $C > C_{cr}$ Fiber and Film	37
d. 30% PBT/70% ABPBI $C > C_{cr}$ Fiber and Film	39
4. Analytical Electron Microscopy	40
a. Energy Dispersive X-ray Analysis	40
b. Electron Energy Loss Spectroscopy	41
c. Microdiffraction	45
5. General Discussion	45
IV SUMMARY AND CONCLUSIONS	50
REFERENCES	52
APPENDIX A: LITERATURE SURVEY ON ELECTRON MICROSCOPY OF POLYMERS	55
APPENDIX B: EFFECTS OF BEAM DAMAGE	65
APPENDIX C: ANALYTICAL ELECTRON MICROSCOPY TECHNIQUES	71

LIST OF ILLUSTRATIONS

FIGURE		PAGE
1	Chemical Structure of PBT and ABPBI Molecules	2
2	Aspect Ratio Schematic	9
3	Detachment Replication Process	14
4	SEM Photo of PBT Fiber Fracture Surface	18
5	SEM Photo of ABPBI Fiber Fracture Surface	18
6	SEM Photo of 30% PBT/70% ABPBI $C > C_{cr}$ Film Fracture Surface	20
7	SEM Photo of 30% PBT/70% ABPBI $C > C_{cr}$ Fiber Fracture Surface	20
8	SEM Photo of 30% PBT/70% ABPBI $C < C_{cr}$ Fiber Fracture Surface	20
9	SEM Photo of 30% PBT/70% ABPBI $C < C_{cr}$ Film Fracture Surface	20
10	WAXD of PBT Fiber	21
11	WAXD of ABPBI Fiber	21
12	WAXD of 30% PBT/70% ABPBI $C > C_{cr}$ Fiber	22
13	WAXD of 30% PBT/70% ABPBI $C > C_{cr}$ Film	22
14	WAXD of 30% PBT/70% ABPBI $C < C_{cr}$ Fiber	22
15	WAXD of 30% PBT/70% ABPBI $C < C_{cr}$ Film	22
16	WAXD Equatorial Scans of As-spun and Heat-treated PBT, ABPBI, and 30% PBT/70% ABPBI $C < C_{cr}$ Fiber	30
17	TEM of PBT Fiber	32
18	TEM of ABPBI Fiber	32
19	TEM of 30% PBT/70% ABPBI $C > C_{cr}$ Fiber	33
20	TEM of 30% PBT/70% ABPBI $C > C_{cr}$ Film	33
21	TEM of 30% PBT/70% ABPBI $C < C_{cr}$ Fiber	34
22	TEM of 30% PBT/70% ABPBI $C < C_{cr}$ Film	34
23	Energy Dispersive X-ray Spectra from 30% PBT/70% ABPBI $C > C_{cr}$ Fiber	42

LIST OF ILLUSTRATIONS (Concluded)

FIGURE		PAGE
24	Sulfur X-ray Map of 30% PBT/70% ABPBI $C > C_{cr}$ Film	43
25	Electron Energy Loss Spectra from 30% PBT/70% ABPBI $C > C_{cr}$ Film	44
26	Microdiffraction Pattern from a Particle in 30% PBT/70% ABPBI $C > C_{cr}$ Film	46
27	Diffraction Intensity vs. Electron Dose for Various SAED Reflections of PBT and ABPBI	
28	Energy Dispersive X-ray Spectra for PBT	
29	Energy Dispersive X-ray Spectra for ABPBI	
30	Electron Energy Loss Spectra for PBT	
31	Electron Energy Loss Spectra for ABPBI	

LIST OF TABLES

TABLE		PAGE
1	Information Obtained from Various Characterization Techniques	4
2	Unit Cell Parameters for ABPBT, ABPBO, and ABPBI	6
3	Mechanical Testing Results for PBT, ABPBI, and 30% PBT/70% ABPBI Fiber and Film	10
4	The d-spacings for PBT, ABPBI, and 30% PBT/70% ABPBI Fiber and Film from WAXD Patterns	24
5	Lateral Crystallite Sizes, D, and Crystallite Orientation Factors, f_x , of PBT, ABPBI, and 30% PBT/70% ABPBI Heat-treated Fiber from WAXD Diffractometer Scans	24
6	The d-spacings for PBT, ABPBI, and 30% PBT/70% ABPBI Fiber and Film from TEM SAED Patterns	35
7	Average Lateral Crystallite Size for PBT, ABPBI, and 30% PBT/70% ABPBI Fiber and Film from TEM Dark Field Images	35

LIST OF ABBREVIATIONS

ABPBI	Poly-2,5(6)benzimidazole
AEM	Analytical electron microscopy
BF	Bright field
C _{cr}	Critical concentration
DF	Dark field
EDS	Energy dispersive x-ray spectroscopy
EELS	Electron energy loss spectroscopy
eV	Electron volts
GPa	Gigapascals
ksi	Kilopounds per square inch
kV	Kilovolts
MPa	Megapascals
Mpsi	Megapounds per square inch
PBT	Poly(p-phenylene benzobisthiazole)
PE	Polyethylene
PPTA	Poly(p-phenylene terephthalamide) (Kevlar TM)
PSt	Polystyrene
PVC	Poly vinyl chloride
SAED	Selected area electron diffraction
SEM	Scanning electron microscopy/microscope
STEM	Scanning transmission electron microscopy/microscope
TEM	Transmission electron microscopy/microscope
WAXD	Wide angle x-ray diffraction

SECTION I

INTRODUCTION

1. CONCEPT OF A MOLECULAR COMPOSITE

A molecular composite is defined here as a polymeric material consisting of two or more components which are dispersed at the molecular level at a scale no greater than a few nm. The two components studied in this investigation are poly(p-phenylene benzobisthiazole), (PBT), and poly-(2,5(6)benzimidazole), (ABPBI). PBT is a rigid-rod, extended chain, aromatic heterocyclic polymer with high strength, high modulus, and excellent environmental and thermal resistance. ABPBI is an aromatic heterocyclic semi-flexible coil polymer with excellent thermal and mechanical properties (Reference 1). The chemical structures for PBT and ABPBI are shown in Figure 1. ABPBI can assume a coil-like structure due to off-axis rotations about its backbone bonds. In contrast, PBT has on-axis bond rotations resulting in extended rigid-rod molecules. The purpose of forming a molecular composite of these two polymers is to reinforce the more ductile, coil-like ABPBI with the stiff, strong, rigid-rod PBT. A molecular composite offers advantages over a macroscopic composite (e.g., chopped glass-fiber reinforced epoxy) in that there are no interfacial adhesion problems or thermally-induced macroscopic stresses due to thermal expansion coefficient differences. Also, processing of rigid-rod PBT in the molecular composite form allows its orientation to be controlled. This orientation control, coupled with composition control, enables mechanical properties to be custom-tailored to an application.

2. CHARACTERIZATION TECHNIQUES

Some of the major techniques which have been used to study pure PBT, pure ABPBI, and a 30% PBT/70% ABPBI blend are mechanical testing, wide-angle x-ray diffraction (WAXD), scanning electron microscopy (SEM), and transmission electron microscopy (TEM). Mechanical testing provides information about the modulus, strength, and ductility of materials. WAXD gives information from a bulk sample about its unit cell parameters, crystallite size and disorder, and orientation. SEM images show surface morphology of a bulk sample down to a resolution of about 20 nm. This is useful for applications such as determining sizes and shapes of phases. TEM can be used for imaging to investigate the structure and morphology of a thin sample section down to a resolution of approximately 3 nm. This technique can be used to

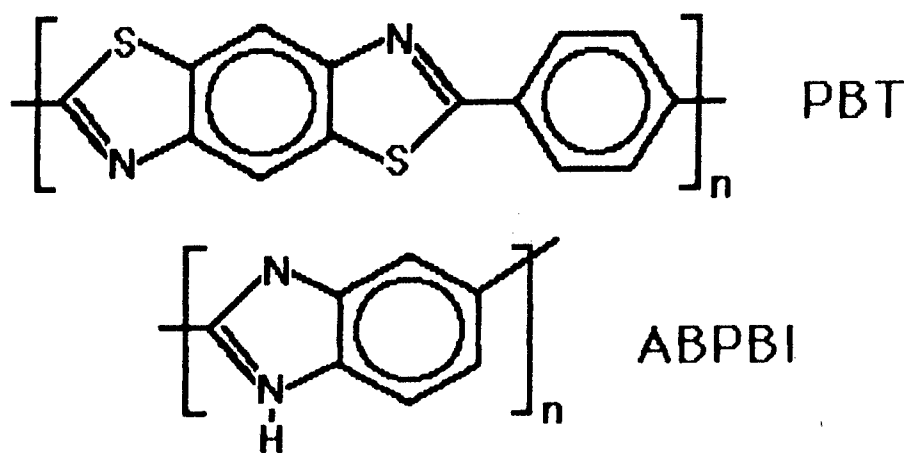


Figure 1. Chemical Structure of PBT and ABPBI Molecules

determine the size, shape, and orientation of crystallites present in the film. TEM can also be used in the selected area electron diffraction (SAED) mode. This technique yields information about unit cell parameters, crystallite size and disorder, and orientation in a thin sample. Table 1 compares the types of data and information available from these techniques. A literature survey on electron microscopy of polymers is presented in Appendix A.

3. PREVIOUS STUDIES

a. PBT Fiber

The structure, morphology, and properties of PBT fiber have been extensively studied by Thomas et al. (Reference 2), Minter (Reference 3), and Allen (Reference 4). The unit cell structure of PBT was proposed by Roche et al (Reference 5) and refined by Odell et al (Reference 6). The non-primitive unit cell is monoclinic with axis lengths of $\underline{a} = 1.196$ nm, $\underline{b} = 0.355$ nm, and $\underline{c} = 1.235$ nm, and a unit cell angle of $\gamma = 100.9^\circ$. The PBT molecular axis is parallel to the \underline{c} axis and the molecules are located in the corners and center of the unit cell. For an individual PBT molecule, the plane of the benzobisthiazole ring structure is about -5° from the \underline{a} axis and the phenylene plane is about 25° from the \underline{a} axis. The relative rotation between the two PBT molecules in the unit cell is uncertain but small. WAXD (References 2,3,4) and SAED (References 2,3,4,5) results have shown that spun, drawn, and heat treated PBT fibers have very high molecular and crystallite orientation. Thomas et al (Reference 7) modelled the positions and intensities of meridional (00ℓ) reflections of SAED patterns on the basis of the Fourier transform of the ordered molecular repeat unit. They found good agreement with experimental patterns demonstrating that there is high molecular orientation in PBT fibers. Minter (Reference 3) reported that only ($hk0$) equatorial reflections in SAED patterns were from crystalline material. The (00ℓ) meridional reflections were from the periodicity of the repeat unit along the molecular axis. The absence of ($hk\ell$) off-axis reflections indicated that the "crystallites" imaged from ($hk0$) reflections were not three dimensionally (3-D) ordered. The molecules were only 2-D laterally ordered and were axially disordered. However, Roche et al (Reference 5) reported faint, smeared ($hk\ell$) reflections in PBT electron diffraction patterns, indicative of limited three-dimensional ordering. Shimamura et al. (Reference 8) also showed by using TEM lattice fringe imaging that PBT contains a limited number

TABLE 1

INFORMATION OBTAINED FROM VARIOUS CHARACTERIZATION TECHNIQUES

<u>Technique</u>	<u>Raw Data</u>	<u>Information</u>
Mechanical testing	Stress-strain curves	Modulus, tensile strength, percent elongation to break
WAXD	Flat plate Laue photo, diffractometer line scan	Crystallite size & disorder, orientation, d-spacings
SEM liquid nitrogen fracture surface	50X to 50,000X image	Fibril morphology, ductility; sizes and shapes of phases
TEM imaging	Bright & dark field images	Morphology; crystallite size & shape
TEM SAED	Selected area electron diffraction pattern	Crystallite size & disorder, orientation, d-spacings

of locally 3-D ordered regions. Minter (Reference 3) used TEM to show that heat-treated PBT fibers contained crystallites about 15 nm long by 10 nm wide, while as-spun PBT fibers had much smaller crystallites (on the order of 2 nm or less). In general these authors reported that the high molecular and crystallite orientation along the fiber axis contributed to very high mechanical properties (References 2,3,4,5). Allen (Reference 4) studied the effect of heat treatment on as-spun PBT fibers and reported moduli up to 280 GPa and tensile strengths up to 2.7 GPa for the heat-treated film.

b. ABPBI Fiber

ABPBI has not been studied as extensively as PBT. The unit cell structure of ABPBI has not been reported. However, the unit cells of the polymers poly 2,6-benzothiazole (ABPBT) and poly 2,5-benzoxazole (ABPBO) have been reported by Fratini et al (Reference 9). They have orthogonal unit cells which are pseudo-orthorhombic. On the basis of the similarity of the chemical structure of ABPBI to that of ABPBT and ABPBO, a preliminary crystal structure has been proposed for ABPBI with an orthorhombic unit cell with axis lengths $a = 0.716$ nm, $b = 0.349$ nm, and $c = 1.17$ nm. A monoclinic unit cell is also not unreasonable for the crystal structure of ABPBI (Reference 10). The unit cell parameters for ABPBT, ABPBO, and ABPBI are listed in Table 2. WAXD was used by Price (Reference 11) to determine the effect of processing on changes in d-spacings in ABPBI. It was found that stretching of ABPBI film caused negligible changes in d-spacings but produced higher orientation. When as-spun fibers of ABPBI were heat treated, the length of the a axis was reduced from 0.83 nm to 0.72 nm, which indicated that molecules were packed more tightly along the a axis. The other unit cell dimensions did not change significantly during heat treatment. Additionally, 3-D order in ABPBI was indicated by the presence of (hkl) reflections. The morphology of ABPBI has not been examined, except for a brief note by Krause and Adams (Reference 12) in which they found 4 nm to 5 nm crystallites in an unoriented heat-treated film of ABPBI. The mechanical properties of ABPBI have been studied by Hwang et al (Reference 13) who reported a modulus of 36.3 GPa and a tensile strength of 1.09 GPa for heat-treated fibers.

c. Polymer Blend Fiber and Film

The concept of a molecular composite and a fabrication method was first suggested in 1978 by Helminiak (Reference 14). Preliminary work on molecular

TABLE 2. UNIT CELL PARAMETERS FOR ABPBT, ABPBO, AND ABPBI

<u>Axis</u>	<u>ABPBT</u>	<u>ABPBO</u>	<u>ABPBI</u>
<u>a</u>	0.604 nm	0.606 nm	0.716 nm
<u>b</u>	0.342	0.338	0.349
<u>c</u>	1.219	1.158	1.17

composites was reported by Husman et al. (Reference 15) in 1980. That study examined the effect of varying the weight ratios of ABPBI/PDIAB (poly(p-phenylene benzodiimidazole)) components in vacuum cast films to determine how morphology, as assessed by SEM and mechanical properties, was related to processing. It was found that reduced phase separation of a phase rich in rod-like molecules produced higher values of mechanical properties. Takayanagi (Reference 16) studied several stiff chains/flexible-coil polymer blends. It was reported that the blend with the finest dispersion of the reinforcing phase had 30 nm-diameter microfibrils of poly(p-phenylene terephthalamide) (PPTA) in a matrix of nylon 6. Takayanagi (Reference 16) suggested a finer dispersion was achieved for a composite of Aramid block copolymer and nylon 6, but the size of the dispersed phase was not quantified.

Hwang et al (Reference 13) investigated solution properties, processing, and mechanical properties of PBT/ABPBI blends. Various weight ratios of PBT/ABPBI were mixed in differing concentrations of polymer in a solvent of methanesulfonic acid. It was found from optical microscopy that when the total concentration of the polymer in the solvent was above a critical concentration ($C > C_{cr}$), liquid crystalline domains appeared within an optically isotropic phase. This demonstrated that phase separation had occurred. The critical concentration varied from 2% to 6% polymer in solution, depending on the ratio of PBT to ABPBI. The critical concentration decreased as the ratio of PBT to ABPBI increased, since there was less ABPBI to inhibit phase separation. The critical concentration decreased as the temperature decreased and also as the molecular weight of PBT increased. It was calculated that an increasing percentage of PBT molecules would be located in the liquid crystalline domains as the polymer concentration increases above C_{cr} . When films were prepared from 30% PBT/70% ABPBI $C > C_{cr}$ solutions SEM images showed the presence of ellipsoidal micron-sized particles in a matrix material. This demonstrated that phase separation in the liquid state persisted during

solidification of the solution into the solid state. SEM backscattering studies of the films indicated that the ellipsoidal particles were composed chiefly of PBT, since the particles had a higher electron backscattering coefficient was due to the presence of a greater amount of sulfur in the particles than in the matrix. The presence of a greater amount of sulfur in the particles was due to a greater amount of sulfur-rich PBT in the particles, although residual solvent could also contribute to the backscattering. It was also asserted that the ellipsoidal particle shape would be expected since the rod-like geometry of the PBT molecules caused them to align side by side in elongated liquid crystalline domains. A note by Krause and Adams (Reference 12) reported that TEM dark field imaging and SAED showed that the particles were chiefly composed of aggregates of 100 nm PBT crystallites. The molecules and crystallites were moderately well aligned with the longitudinal axis of the ellipsoids.

The phenomenon of phase separation has important consequences with regard to its effects on mechanical properties of polymer composites. In macroscopic composite theory the effects of the geometry of reinforcing phase can be evaluated in terms of a parameter known as the aspect ratio. The aspect ratio is defined as $2L/D$, where L is the length and D is the diameter of the reinforcing phase. For efficient reinforcement, simple macroscopic composite mechanics theory states that the aspect ratio of the reinforcing phase should be at least 100 (Reference 17).

It has been proposed that the effect of reinforcement of a ductile polymer matrix by rigid rod molecules is analogous to the reinforcing effect of high aspect ratio fibers on the properties of macroscopic composites (Reference 13). If we consider that the rigid rod PBT molecules can be dispersed singularly or in small bundles in an ABPBI matrix, this would produce a high aspect ratio of the reinforcing phase, resulting in efficient reinforcement of the matrix material. The aspect ratio of PBT molecule may be as high as 400, since its length is about 120 nm while its diameter is about 0.6 nm. Even in bundles of PBT molecules 2 nm to 3 nm wide, a high aspect ratio of 80 to 120 would be maintained. The high aspect ratio, which would result if rigid rod PBT molecules were well dispersed as individual molecules or small molecular bundles is shown schematically in Figure 2a.

If, alternatively, rigid rod molecules phase separate on a large scale from the matrix material, then the aspect ratio of the rigid rod reinforcing phase would be

reduced to low values. The low aspect ratio of the reinforcing phase would provide inefficient reinforcement of the matrix material. This is shown schematically in Figure 2b.

The effects of phase separation on mechanical properties were studied in PBT/PDIAB blends by Husman et al. (Reference 15) and in PBT/ABPBI blends by Hwang et al (Reference 13). In both studies, it was found that vacuum cast film contained ellipsoidal particles 2 to 4 microns long located in matrix material. The removal of solvent during the casting process caused the polymer concentration in the solvent to rise above C_{cr} and induce phase separation. The phase separation was manifested in the formation of the second-phase particles. By using evidence from mechanical testing, SEM, and WAXD, it was proposed that these particles were chiefly composed of rigid-rod PBT molecules which were agglomerated into aggregates of low aspect ratio. It was also shown that the low values of mechanical properties observed for the vacuum cast films were due to poor reinforcement of the matrix material by the low aspect ratio of the aggregates.

Processing of PBT/ABPBI blends from $C < C_{cr}$ solutions was studied by Hwang et al (Reference 13) and Kulshreshtha and Price (Reference 18). It was found that when $C < C_{cr}$ solution was extruded as fiber or film and then rapidly coagulated in water, large scale phase separation was prevented. After oven drying of the fibers and films no phase-separated aggregates were observed with SEM to its resolution limit of 20 nm. It was concluded, by using mechanical property measurements of oriented fibers of homopolymer components and of the blends, that a molecular composite had been achieved by processing fibers from a $C < C_{cr}$ solution. Wellman et al (Reference 19) used WAXD, light scattering, and optical microscopy to conclude that the PBT in a $C < C_{cr}$ 40% PBT/60% ABPBI blend was dispersed into very small bundles.

The mechanical testing results for fiber and film of PBT, ABPBI, and $C > C_{cr}$ and $C < C_{cr}$ blends are presented in Table 3 (References 13, 15, 20). The $C > C_{cr}$ material was oven dried and not heat-treated. The results show that the properties of the fiber processed from $C < C_{cr}$ solution have values which are intermediate between the values for PBT and ABPBI fibers. The $C < C_{cr}$ fiber has a modulus ten times that of the $C > C_{cr}$ fiber and a tensile strength four times that of the $C > C_{cr}$ fiber. This was reported to be due to both the finer dispersion of the reinforcing phase and also higher orientation achievable when processing the polymer blend from $C < C_{cr}$ solutions (Reference 13).

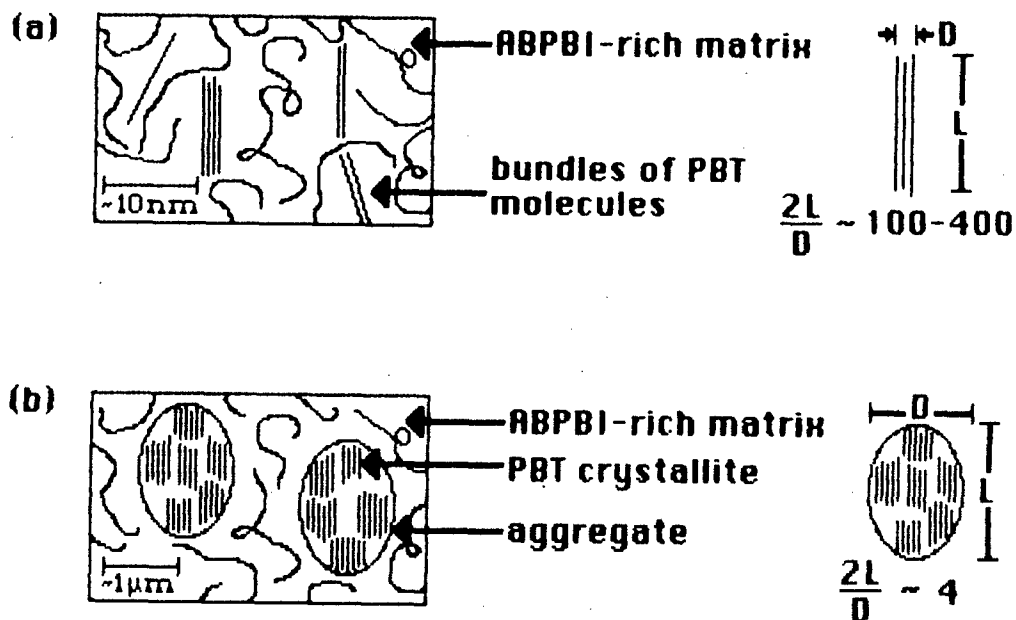


Figure 2. Aspect Ratio Schematic (a) Well-dispersed PBT molecules or molecular bundles yield a high aspect ratio (b) Phased-separated aggregates yield a low aspect ratio

TABLE 3. MECHANICAL TESTING RESULTS PBT, ABPBI, AND 30% PBT/70% ABPBI FIBER AND FILM

<u>Sample</u>	<u>Modulus</u>	<u>Tensile Strength</u>	<u>Elongation to Break</u>
PBT fiber	265 GPa 38 Mpsi	2800 MPa 400 ksi	1.1 %
ABPBI fiber	36 GPa 5.3 Mpsi	1090 MPa 158 ksi	5.2 %
30% PBT/70% ABPBI C>C _{cr} fiber	11 GPa 1.6 Mpsi	310 MPa 45 ksi	13 %
30% PBT/70% ABPBI C>C _{cr} film	1.1 GPa 0.16 Mpsi	35.1 MPa 5.1 ksi	5.6 %
30% PBT/70% ABPBI C<C _{cr} fiber	117 GPa 17 Mpsi	1270 MPa 184 ksi	1.4 %
30% PBT/70% ABPBI C<C _{cr} film	88 GPa 13 Mpsi	918 MPa 132 ksi	2.4 %

4. OBJECTIVES

In the previous studies discussed above, SEM and mechanical testing results indicated that, with appropriate processing conditions, a molecular composite fiber or film had been formed. However, there was no direct morphological confirmation for the dispersion of the reinforcing phase at a scale finer than 20 nm, nor was there quantification of orientation in fibers and films. Additionally, for phase-separated samples, information about the composition and structure of the phase-separated particles was only indirectly determined from SEM results.

The goal of this study was to use electron microscopy and x-ray diffraction techniques to examine the structure and morphology of fibers and films of pure PBT and ABPBI, and also of the PBT/ABPBI blends processed from C>C_{cr} and C<C_{cr} solutions. SEM was used to examine the morphology of sample fracture surfaces. WAXD was used to measure d-spacings, crystallite size, and crystallite orientation. TEM dark field imaging and selected area electron diffraction (SAED) modes were used to examine morphology, d-spacings, and crystallite size and orientation of these fibers and films. Analytical electron microscopy (AEM) techniques of energy dispersive spectroscopy (EDS), electron energy loss spectroscopy (EELS), and

microdiffraction were used to provide information about structure and composition of the fibers and films. The structure and morphology results were correlated to the earlier results of mechanical properties studies.

SECTION II

EXPERIMENTAL METHODS

1. MATERIALS PROCESSING

The processing of PBT, ABPBI, and PBT/ABPBI blends into fiber and film was reported in detail by Hwang et al (Reference 13) and is briefly summarized here. The molecular weights were estimated by intrinsic viscosity measurements to be 41 kg/mole for PBT and 100 kg/mole for ABPBI. A mixture of 97.5 volume percent methanesulfonic acid (MSA) and 2.5 volume percent chlorosulfonic acid (CSA) was the solvent for the polymers. The amount of PBT and ABPBI in the solution varied from 2 to 4%, with C_{cr} being 3.1% at room temperature.

The processing of vacuum cast film was described by Husman et al. (Reference 15). Solvent from $C < C_{cr}$ solution was removed in a sublimator, with the decreasing amount of solvent resulting in $C > C_{cr}$ solution and film. The film was subsequently dried in a vacuum oven to remove residual solvent and improve mechanical properties.

Fibers were spun (Reference 13) by extruding solution through a spinneret die into a coagulating water bath. The fibers were dry spun, usually to a high draw ratio, in the air gap between the die and the water bath. Films were solution extruded through a slot die into a coagulating water bath. The wet fiber or film was neutralized in NH_4OH overnight and rinsed in distilled water. The $C > C_{cr}$ fiber was oven dried. The fibers and films produced from $C < C_{cr}$ solution were heat treated under tension at elevated temperatures in air.

2. SAMPLE PREPARATION

Samples were prepared for SEM examination by submerging fiber and film in liquid nitrogen and then fracturing. A sample was then sputter-coated with gold-palladium to prevent charging when imaging.

WAXD fiber samples were prepared by winding approximately 100 cm of a single filament around a cardboard holder, yielding fiber bundles with diameters from about 0.25 mm to 0.7 mm. WAXD film samples required no special preparation techniques.

For TEM the principal technique used to produce very thin samples was detachment replication, described previously by Minter (Reference 3). Ion thinning and ultramicrotomy were also used as auxiliary techniques for samples not amenable to preparation by detachment replication. The thinnest possible samples were prepared to allow resolution of smaller features in the samples.

The detachment replication process is schematically illustrated in Figures 3a to 3d. A solution of about 20% by weight of collodion in amyl acetate was prepared. A layer of this solution of about 20x10x2 mm was placed by pipette onto a clean glass slide and allowed to dry for 20 to 40 minutes until it was tacky. Pieces of the sample about 1 cm long were laid on the collodion solution with a few mm of sample hanging over the edge of the collodion (to facilitate later removal). The sample displaced a little collodion without being completely embedded (Figure 3a). After drying overnight, a sample was carefully peeled from the collodion, leaving microscopic fibrils of the sample stuck in the grooves. The quality of the detached sample material was checked by examining the grooves with an optical microscope at a magnification of about 300 (Figure 3b). Grid-sized (3mm) squares containing these fibril-filled grooves were cut and lifted off the slide. They were placed onto holey-carbon grids on a mesh screen inside a covered petri dish which was filled with amyl acetate to the level of the screen (Figure 3c). The amyl acetate dissolved the collodion overnight allowing the sample to settle onto the grid. After the grid was dried on filter paper, it was optically inspected to make sure some sample was in place and ready for TEM study.

The copper mesh grids that were used were covered with holey-carbon film (Figure 3d). The holey carbon film provided extra support and reduced charging of the sample by the electron beam. Typically, the carbon film had 0.5 to 5.0 μm holes on a 100 - 200 mesh (per inch) copper grid.

Detachment replication worked well on samples with a fibrillar nature. However, routine detachment replication did not produce good samples for less fibrillar material, such as $\text{C} > \text{C}_{\text{cr}}$ fiber. The surface of these samples was roughened with a razor blade to improve the chances of detaching a thin section although at a risk of inducing artifacts from deformation.

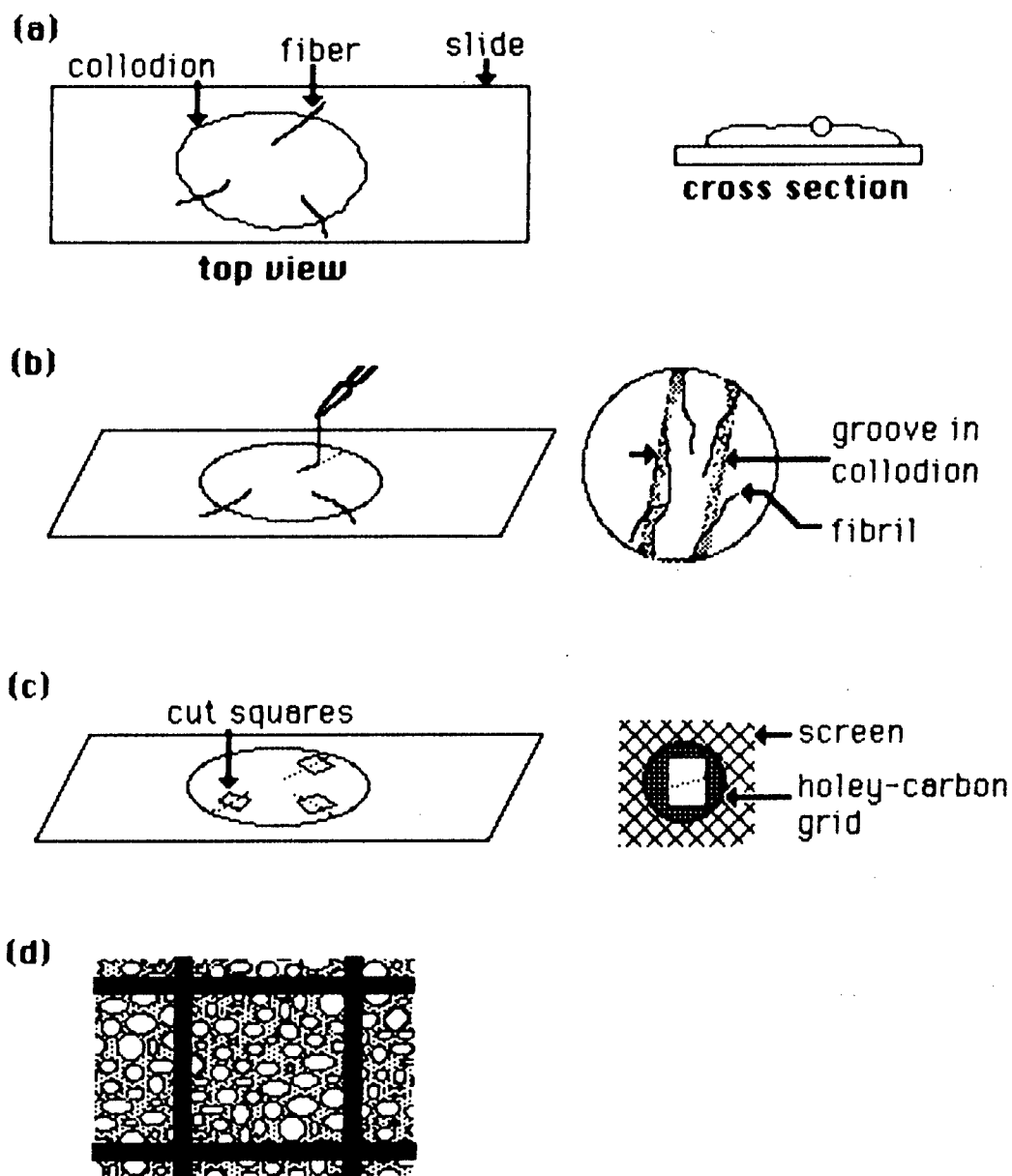


Figure 3. Detachment Replication Process (a) The placement of samples on collodion (b) Peeling samples off collodion (c) Cutting and placement on grid of collodion squares (d) Magnification of typical holey carbon grid

3. EQUIPMENT AND OPERATION

a. Scanning Electron Microscopy

Sample fracture surfaces were imaged on an ISI Alpha 9 scanning electron microscope at 10KV at magnifications from 100X to 5000X. Images were recorded on Polaroid P/N 55 film.

b. Wide Angle X-ray Diffraction

The WAXD photographs were recorded with flat-film Statton (Worhus) cameras. CuK_α radiation was generated by an Elliot GX20 rotating anode x-ray generator with a nickel filter. The sample-to-film distances were 29.2 ± 0.2 mm for the two Statton cameras, calibrated by the known crystalline reflections of a standard silicon powder, SRM 640.

The WAXD diffractometer scans were collected on a Picker FACS-1 automated diffractometer. A copper tube with a graphite crystal incident beam monochromator was used to obtain CuK_α x-rays. One millimeter incident beam and diffracted beam collimators were used. The crystallite orientation in various samples was calculated according to the Hermans-Stein orientation function using data from azimuthal scans, and crystallite dimensions were calculated from the Scherrer equation using the line breadth measurements from equatorial scans, in a manner similar to that reported by Minter (Reference 3). Since the effect of disorder was not included, the crystallite size determined represents the minimum bound. The take-off angle and symmetrically variable aperture were selected to optimize crystallite size measurements. Hexamethylenetetramine ($\text{C}_6\text{H}_{12}\text{N}_4$) was used as a standard to correct for instrumental line broadening.

c. Transmission Electron Microscopy

TEM imaging and SAED were performed on a JEOL 100CX using an accelerating voltage of 100 to 120 kV. Micrographs were taken on Kodak SO-163 film.

Polymers are susceptible to beam damage by the transfer of energy from the electrons to the sample. This can produce artifacts by structural changes, such as loss of crystallinity. Beam damage of samples was minimized by keeping the beam intensity low and the time the sample was exposed to the beam as short as possible. Fortunately, PBT and ABPBI are relatively resistant to beam damage. Minter

(Reference 3) reported that the maximum magnification for bright field micrographs of undamaged PBT is 140,000x, an order of magnitude higher than the value for polyethylene. A study of the effect of beam damage on electron microscopy results for the PBT/ABPBI system is presented in Appendix B.

Minimum dose techniques, as described by Minter (Reference 3) were used to examine samples and are briefly summarized here. Samples were scanned in the bright field imaging mode at a low magnification (typically 2600x) with the beam spread out. When a promising area was located, it was examined at a higher magnification (typically 10,000x to 20,000x) with the beam slightly converged. The selected area electron diffraction (SAED) mode was used at low emission current to locate an area on the sample with a diffraction pattern with sharp reflections. A prominent equatorial reflection of the SAED pattern was tilted into the objective aperture so that the remainder of the reflections in the pattern were masked. The dark field tilted beam image was then observed after removing the field limiting aperture. The beam was then turned off and the sample was translated to a fresh adjacent undamaged area. Finally, a plate of film was exposed as soon as the beam was turned on.

d. Analytical Electron Microscopy

Samples were examined by analytical electron microscopy on a JEOL 100CX with STEM/AEM capabilities, using an accelerating voltage of 100 kV. Background information on AEM techniques is given in Appendix C. Results of the beam damage study in Appendix B were obtained on a Philips 400T STEM operated at 120 kV. Energy dispersive x-ray spectra were obtained on a JEOL JSM 840 with a Si(Li) detector and a Tracor Northern multichannel analyzer using acquisition times of 20-50 seconds. Electron energy loss spectra were obtained with a JEOL spectrometer and a Tracor Northern multichannel analyzer using acquisition times of 15-30 seconds. For the beam damage study in Appendix B, the electron energy loss spectra were collected with a Gatan spectrometer on a Philips 400T STEM.

SECTION III

RESULTS AND DISCUSSION

1. SCANNING ELECTRON MICROSCOPY IMAGING

A PBT fiber fracture surface imaged by SEM is shown in Figure 4. The PBT fiber was dry-jet wet spun and heat treated. The fracture surface contains many partially separated fibrils over 10 μm long and about 0.3 μm in diameter. This indicates that molecular orientation along the fiber axis is high, and that the fiber has much higher strength along the fiber axis than transverse to it. The absence of micronecking, drawing or other plastic deformation features indicates that the fiber has little ductility.

An ABPBI fiber fracture surface is shown in Figure 5. The ABPBI fiber was also dry jet wet spun and heat treated. Some pieces of the fiber are drawn and stretched and recoiled into clumps, indicating a moderate ductility. Extensive fibrillation, as seen in PBT fiber, is not observed for the ABPBI fiber, indicating that its ductility and lateral strength are higher than for the PBT fiber and also that it may not be as well oriented as the PBT fiber.

The fracture surface of the 30% PBT/70% ABPBI $C > C_{cr}$ vacuum cast film is shown in Figure 6. The film was oven dried, but not heat treated at an elevated temperature. The fracture surface shows ellipsoidal particles 2 to 4 μm long, sometimes fractured, located in a matrix material which has substantial dimpling. The particles are not tightly bound to the matrix, and fractured surfaces of some particles indicate that they are relatively brittle compared to the matrix. The dimpling of the matrix is due to micronecking associated with plastic deformation and indicates that the matrix has considerable ductility. The elongated shape of the particles is probably due to PBT molecules aligned along the longitudinal axis of the particles. Additional evidence which indicates that the particles are aggregates which are composed chiefly of PBT molecules is the presence of many fractured particles. It was previously shown that PBT fibers have little ductility compared to ABPBI fibers. These observations which indicate the particles are chiefly composed of PBT are consistent with SEM studies of Hwang et al (Reference 13).

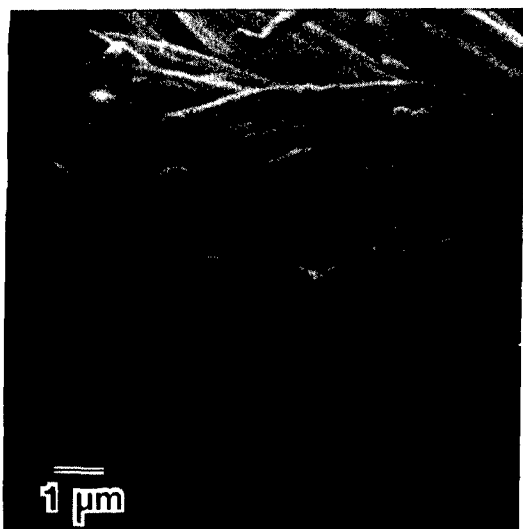


Figure 4. SEM Photo of PBT Fiber Fracture Surface

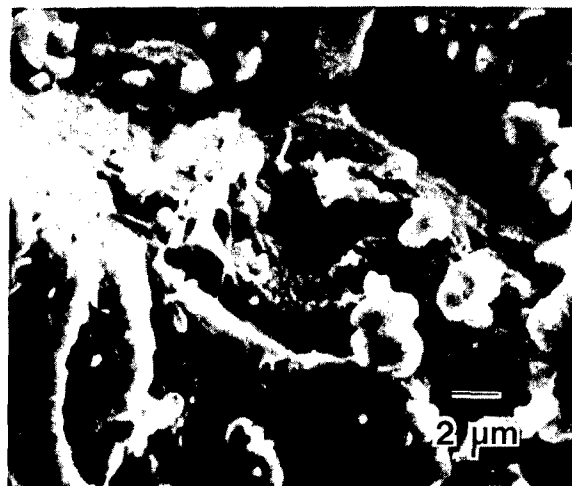


Figure 5. SEM Photo of ABPBI Fiber Fracture Surface

The fracture surface of a 30% PBT/70% ABPBI fiber spun from $C > C_{cr}$ solution is shown in Figure 7. The fiber was oven dried but not heat treated at an elevated temperature. Round and ellipsoidal particles 0.2 to 0.4 μm in size are prevalent throughout the matrix material. The matrix shows moderate drawing, indicating a moderate ductility. The lack of fibrillar features indicates the matrix has little or no orientation. The small particles in the fracture surface resemble the larger PBT-rich aggregates discussed previously in the $C > C_{cr}$ phase-separated film. Since the fiber was processed from $C > C_{cr}$ solution, phase separation had already occurred prior to spinning of the fibers. It is likely that shearing of the solution during fiber spinning reduced the size of the phase separated regions, probably to the scale observed for the particles in the film. The size of the phase-separated particles would then be preserved during coagulation of the fiber in the water bath. From this information it is concluded that the small round and ellipsoidal particles in the $C > C_{cr}$ fiber fracture surface are composed chiefly of domains of PBT molecules broken or sheared into small phase-separated PBT-rich aggregates.

The 30% PBT/70% ABPBI $C < C_{cr}$ fiber was spun from $C < C_{cr}$ solution. It was also wet drawn, neutralized, and heat treated. The micrograph of its fracture surface is shown in Figure 8. The fiber fracture surface contains fibrils 1 to 10 μm long and 0.1 to 0.5 μm in diameter and also shows some limited drawing. This indicates that there is moderately high molecular orientation along the fiber axis. The drawing indicates there is limited ductility. The fiber does not contain any aggregates to the 20 nm resolution limit of the SEM. This places an upper size limit of 20 nm on any possible phase separation in the fiber.

The 30% PBT/70% ABPBI $C < C_{cr}$ film was extruded from $C < C_{cr}$ solution. It was neutralized and heat treated. The micrograph of its fracture surface is shown in Figure 9. The fracture surface shows little fibrillation or stretching. This indicates the film has little orientation and limited ductility. As with the fiber, no aggregates are observed in the film down to the 20 nm resolution limit of the SEM, thus placing an upper size limit of 20 nm on possible phase separation in the film.

2. WIDE ANGLE X-RAY DIFFRACTION

The WAXD photographs for samples in this study are shown in Figures 10 to 15. The d-spacings for heat-treated fiber samples have been determined from measurements

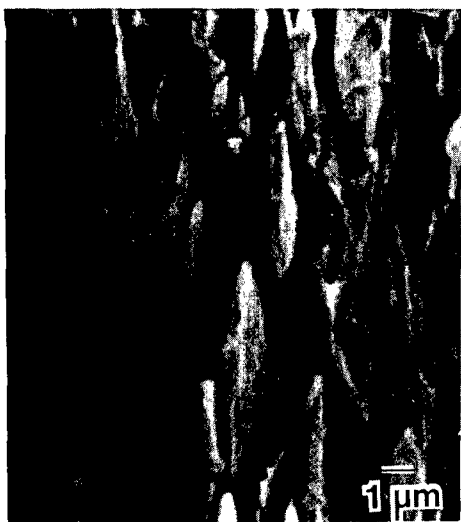


Figure 6. SEM Photo of
30% PBT/70% ABPBI $C > C_{cr}$ Film
Fracture Surface

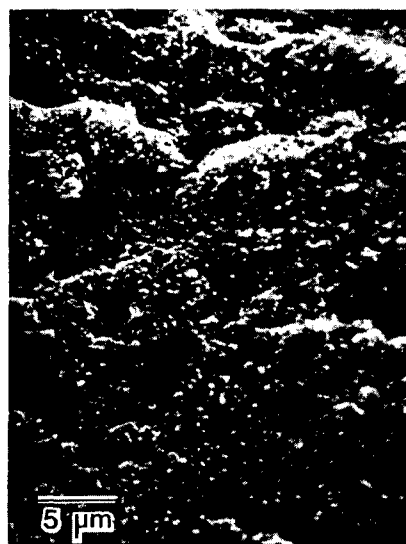


Figure 7. SEM Photo of
30% PBT/70% ABPBI $C > C_{cr}$ Fiber
Fracture Surface

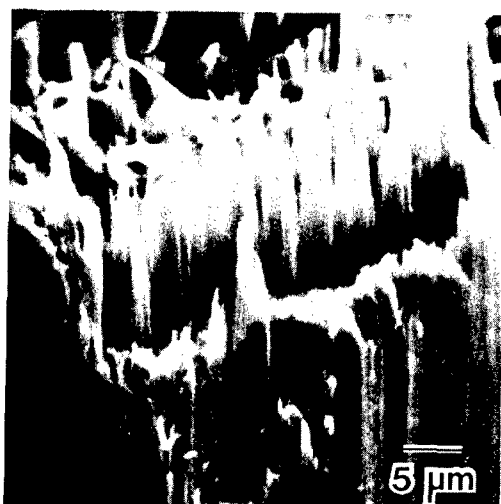


Figure 8. SEM Photo of
30% PBT/70% ABPBI $C < C_{cr}$ Fiber
Fracture Surface



Figure 9. SEM Photo of
30% PBT/70% ABPBI $C < C_{cr}$ Film
Fracture Surface

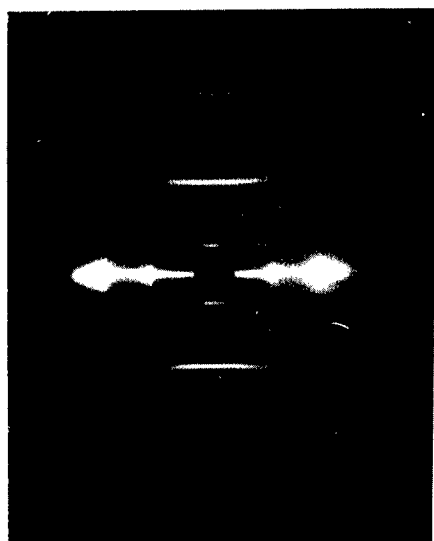


Figure 10. WAXD of PBT Fiber

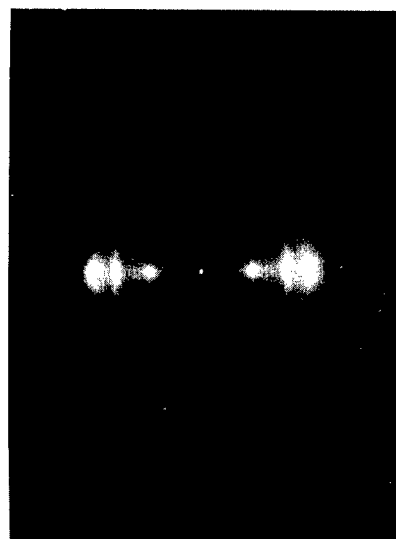


Figure 11. WAXD of ABPBI Fiber

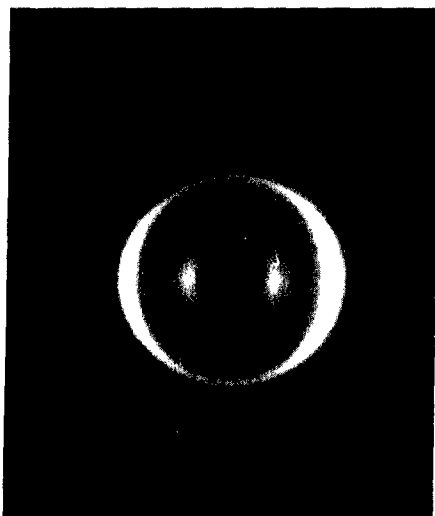


Figure 12. WAXD of
30% PBT/70% ABPBI $C > C_{cr}$ Fiber

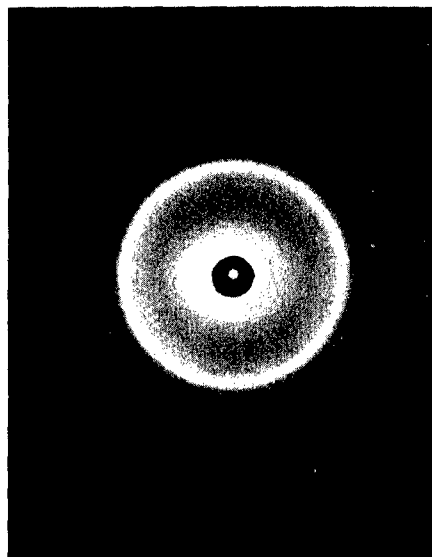


Figure 13. WAXD of
30% PBT/70% ABPBI $C > C_{cr}$ Film

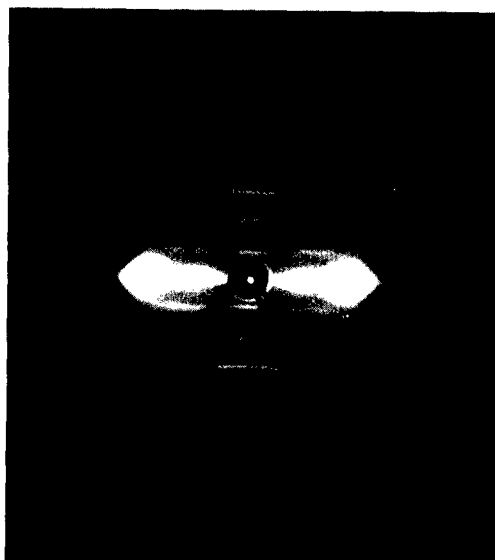


Figure 14. WAXD of
30% PBT/70% ABPBI $C < C_{cr}$ Fiber

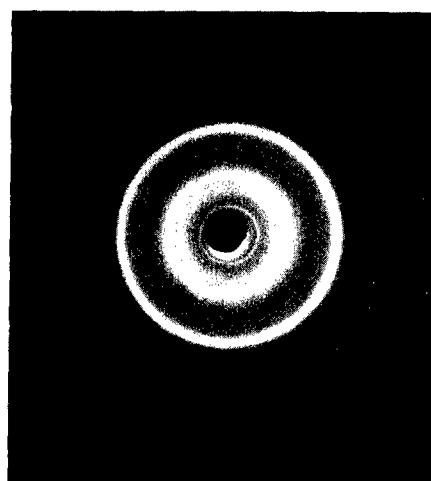


Figure 15. WAXD of
30% PBT/70% ABPBI $C < C_{cr}$ Film

of the positions of the reflections in the photographs and are presented in Table 4. Crystallite sizes in various samples have been determined from analysis of diffractometer line breadth scans and are presented in Table 5. The orientation factor of crystallites has been determined from azimuthal diffractometer scans for various samples, and this data is also presented in Table 5. Perfect orientation of an equatorial reflection perpendicular to the fiber axis is represented by a value of -0.5

a. PBT Fiber

The WAXD pattern for heat-treated PBT fiber shown in Figure 10 shows sharp, well-arc'd equatorial reflections. These features are indicative of large crystallites that are well-oriented along the fiber axis. The pattern also shows sharp, flat meridional reflections extending to the 6th order, which indicates that molecules are highly oriented along the fiber axis. The lack of off-axis (hkl) reflections indicates the diffracting regions have molecules which are laterally ordered, but axially disordered, resulting in two-dimensional (2-D) crystallites (References 3,5). The limited 3-D ordering of PBT crystallites reported in earlier studies (Reference 5) was not observed here.

The dimensions of the crystallites in the PBT fibers, as determined from line breadth analysis, are 8.9 nm (measured from the 0.58 nm reflection) along the a axis and 5.6 nm (measured from the 0.35 nm reflection) along the b axis. This means that the crystallite lateral dimensions are larger in the plane of the heterocyclic rings and smaller in the direction that is perpendicular to the plane of the heterocyclic rings. This gives a "brick"-shaped morphology to the 2-D ordered regions where the length is along the molecular axis and the width of the region is about twice its thickness. In this "brick-shaped morphology, the laterally ordered regions are broader parallel to the heterocyclic rings. This may be due to preferential growth of crystallites during heat treatment. It may also be due to molecules which have slid along the chain axis parallel to the plane of the heterocyclic rings in the liquid crystalline state, when the protonated chains are probably wider than they are in the unprotonated state. This would create either more lateral disorder or smaller crystallite size between heterocyclic rings. The freedom of motion of molecules in the planes of the heterocyclic rings in the liquid crystal state should also permit higher crystallite orientation in that direction during fiber spinning.

TABLE 4. THE D-SPACINGS FOR PBT, ABPBI, AND 30% PBT/70% ABPBI FIBER AND FILM FROM WAXD PATTERNS

	----- 30% PBT/70% ABPBI -----					
	<u>PBT</u> <u>fiber</u>	<u>ABPBI</u> <u>fiber</u>	<u>C>Ccr</u> <u>fiber</u>	<u>C>Ccr</u> <u>film</u>	<u>C<Ccr</u> <u>fiber</u>	<u>C<Ccr</u> <u>film</u>
Equatorial (hko)	--	.72	.83	.83	.74	.74
d-spacings (nm)	.58	--	.60	.60	.61	.60
	--	.45	--	--	.44	--
	.35	.35	.35	.35	.35	.35
	.32	--	--	--	--	--
Off-axis (hkl)	--	.51	--	--	--	--
d-spacings (nm)	--	.43	--	--	--	--
	--	.32	--	--	--	--
Meridional (00l)	1.25	--	--	--	1.27	1.25
d-spacings (nm)	--	(1.17)	--	--	--	--
	.63	--	--	--	} .60	--
	--	.58	--	--		--
	.42	--	--	.42	.42	.42
	--	.39	--	--	.39	--
	.31	--	--	--	.31	--
	--	.29	--	--	--	--
	.24	--	--	.25	.25	.25
	--	(.23)	--	--	.23	--

TABLE 5. LATERAL CRYSTALLITE SIZES, D, AND CRYSTALLITE ORIENTATION FACTORS, f_x , OF PBT, ABPBI, AND 30% PBT/70% ABPBI HEAT-TREATED FIBER FROM WAXD DIFFRACTOMETER SCANS

d-spacing (nm)	<u>PBT</u>		<u>ABPBI</u>		<u>C<C_{cr}</u> 30 %PBT/70% ABPBI	
	<u>D (nm)</u>	<u>f_x</u>	<u>D (nm)</u>	<u>f_x</u>	<u>D (nm)</u>	<u>f_x</u>
.58	8.9	-.41	--	--	--	--
.44	--	--	3.2	-.35	--	-.38
.35	5.6	-.46	2.1	-.41	2.6	-.43

The crystallite orientation factors bear out this interpretation since the b axis (0.35 nm reflection) has an orientation factor of -0.46 while the a axis (0.86 nm reflection) has an orientation factor of -0.41.

b. ABPBI Fiber

The WAXD pattern for heat-treated ABPBI fiber is shown in Figure 11. The equatorial reflections are more diffuse and less strongly arced than the equatorial reflections in PBT fiber. These facts indicate that ABPBI crystallites are smaller and less well-oriented than those in PBT fiber. The meridional reflections extend out to four orders, but are more diffuse and arced than those for the PBT fiber, indicating that molecular orientation in ABPBI is high, but is less than PBT. In contrast to the WAXD photographs for PBT, the ABPBI WAXD photographs shows off-axis (hkl) reflections indicating that 3-D order exists in ABPBI.

The lateral sizes of the ABPBI crystallites are 3.2 nm along the $[110]$ direction (measured from the 0.44 nm reflection) and 2.1 nm along the $[010]$ direction (measured from the 0.34 nm reflection). These lateral crystallite dimensions are much smaller than those for PBT. This is probably due to the fact that the semi-flexible coil molecules of ABPBI do not order as well as the rigid-rod PBT molecules. The orientation factor of the $[110]$ direction (0.44 nm reflection) is -0.35, and of the $[010]$ direction (0.34 nm reflection) is -0.41. The orientation of the crystallites is in general, less for ABPBI than for PBT. Once again this is probably due to the greater difficulty of ordering the semi-flexible coil ABPBI molecules compared to the rigid-rod PBT molecules. This is reasonable since ABPBI is spun from an isotropic solution, whereas the PBT is spun from the liquid crystal solution. However, like PBT, the orientation factor is higher for the $[010]$ direction (0.34 nm reflection), the lateral direction in the plane of which contains the heterocyclic rings in ABPBI. This indicates that, similar to PBT, molecules of ABPBI are more likely to have slid along the chain axis in a plane parallel to the plane of the heterocyclic rings.

c. 30% PBT/70% ABPBI $C > C_{cr}$ Fiber and Film

The WAXD pattern for 30% PBT/70% ABPBI $C > C_{cr}$ fiber is shown in Figure 12. There are three reflections present which are all relatively diffuse and slightly arced. The spacings of the reflections are listed in Table 4. The 0.83 nm

reflection is characteristic of the crystal structure of pure ABPBI fibers which have not been heat treated at high temperatures. The presence of this reflection indicates ABPBI crystallites are present. The 0.60 nm reflection, which is characteristic of the crystal structure in pure PBT fibers, indicates PBT crystallites are present. The 0.35 nm reflection is a composite reflection and is characteristic of both ABPBI and PBT crystal structures. The diffuseness of the reflections indicates crystallites are relatively small and/or disordered. The weak arcing of the reflections indicates the crystallites of both PBT and ABPBI are only slightly oriented. Thus, the fibers of 30% PBT/70% ABPBI spun from $C > C_{cr}$ solution have both PBT and ABPBI crystallites which are relatively small and/or disordered and are only slightly oriented. During processing of these fibers it was not possible to attain a high extrusion rate or a high dry spin ratio to achieve high orientation. This resulted in the limited orientation observed for the PBT and ABPBI crystallites in the fiber. Smaller crystallite sizes are probably due to the lack of molecular ordering through orientation during processing and lower oven heat treatment temperatures. Both factors would inhibit the growth of larger crystallites.

The WAXD pattern for 30% PBT/70% ABPBI $C > C_{cr}$ vacuum cast film is shown in Figure 13. There are four uniform Debye rings present with the d-spacings listed in Table 4. An additional higher angle reflection is present in an overexposed photograph not shown here and is the last reflection listed in the table. The lowest angle reflection at a d-spacing of 0.83 nm, which corresponds to an equatorial reflection in as-spun ABPBI fibers, indicates ABPBI crystallites are present. The 0.60 nm reflection, which corresponds to an equatorial spacing in PBT fibers, indicates PBT crystallites are present. The 0.35 nm reflection is a composite reflection which represents a spacing characteristic of the distance between planes containing heterocyclic rings in both PBT and ABPBI. Additionally, there are 0.42 nm and 0.26 nm reflections which correspond to meridional spacings in pure PBT fibers. The unarced rings indicate there is no overall orientation of crystallites in the bulk fiber.

All reflections from crystallites in the film are relatively diffuse, but somewhat sharper than those in the $C > C_{cr}$ fiber, which indicates crystallites are relatively small (and/or disordered) but are larger (and/or less disordered) than

those in the fiber. This is reasonable since the film was quiescently solidified during vacuum casting and crystallites were not disordered by shearing as were the crystallites in the fiber. This assumption is supported by SEM images which showed the presence of larger (2-4 μm) PBT-rich particles in the 30% PBT/70% ABPBI $C > C_{cr}$ film, compared to the smaller (0.1-0.2 μm) aggregates present in the 30% PBT/70% ABPBI $C > C_{cr}$ fiber. It is also likely that PBT crystallites within particles in the film are larger than those within particles in the fiber. The presence of the additional PBT meridional reflections in the WAXD photographs indicates that order of the PBT molecules is higher in the film than in the fiber. There may be some bending or twisting of PBT molecules which occurs during spinning of the fiber, resulting in some disordering of the periodicity along PBT molecules. This disorder along the PBT molecules would be less likely for PBT in the vacuum cast films.

d. 30% PBT/70% ABPBI $C < C_{cr}$ Fiber and Film

The WAXD pattern for 30% PBT/70% ABPBI $C < C_{cr}$ fiber shown in Figure 14 shows highly-arc'd equatorial reflections, indicating well-oriented crystallites, and flat meridional reflections extending out to high orders, indicating well-oriented molecules of both species. The d-spacings for the reflections are listed in Table 4. This blend fiber has equatorial and meridional spacings present which correspond to those in both PBT and ABPBI fibers. The 0.74 nm equatorial reflection, which is characteristic of an equatorial reflection in heat treated ABPBI fiber, indicates ABPBI crystallites are present. Additionally, there are at least three meridional reflections present (at 0.60 nm, 0.39 nm, and 0.23 nm) which are characteristic of meridional spacings of ABPBI fibers. This indicates that molecules of ABPBI are ordered and highly oriented in the blend fiber. In fact, the meridional reflections characteristic of ABPBI in the blend fiber are actually flatter and sharper than those in the pure ABPBI fiber. This higher orientation of the ABPBI molecules in the blend fiber compared to the pure ABPBI fiber may be a template effect (like epitaxy) of the long, stiff PBT molecules.

In comparing this fiber to the pure ABPBI fiber, the orientation factor for ABPBI crystallites in the [110] direction (0.44 nm reflection) increases from -0.35 to -0.38. The orientation factor of the 0.34 nm reflection is -0.43, but this is a spacing which is present in both PBT and ABPBI and represents an average orientation of crystallites of both PBT and ABPBI. It is interesting that the ABPBI molecular

and crystallite orientation increase in the blend fiber. It has been suggested by Hwang et al (Reference 13) that this is due to the entanglement of flexible-coil ABPBI molecules with the rigid-rod PBT molecules causing an "epitaxial" alignment and ordering of ABPBI molecular segments along PBT molecules during the fiber spinning process. Although the alignment of ABPBI molecules and crystallites increases in the blend fiber, the diffuseness of the characteristic 0.74 nm and 0.44 nm reflection indicates crystallite size remains relatively small. The presence of the PBT molecules probably interferes with the organization of ABPBI molecules into larger crystallites.

The 0.61 nm spacing, which is characteristic of an equatorial reflection in PBT fiber, indicates PBT crystallites are present. Additionally there are at least five meridional reflections present (1.27 nm, 0.60 nm, 0.42 nm, 0.31 nm, 0.25 nm) which are characteristic of meridional reflections of PBT fibers. This indicates that the molecules of PBT are well-ordered in the blend fiber. However, there are not as many orders of meridional reflections, nor are the meridional reflections characteristic of PBT molecules as flat or as sharp, as those in the pure PBT fiber. This indicates that the PBT molecules are less ordered and/or less oriented than in pure PBT fiber. This is probably due to the presence of the semi-flexible coil ABPBI molecules which somewhat inhibit orientation of the rigid-rod PBT molecules during the spinning of the blend fiber. The reduction of the orientation factor of the 0.35 nm composite reflection from -0.46 in pure PBT fiber to -0.43 in the blend fiber generally supports the idea of reduced orientation in the blend fiber. Although the 0.35 nm reflection is a composite reflection from both PBT and ABPBI crystallites, it is not unreasonable to assume, if large-scale phase separation does not occur, that the orientation factor for both the PBT and ABPBI is similar between planes of heterocyclic rings.

A major difference between the PBT in the blend fiber and the pure PBT fiber is the relative diffuseness of the characteristic 0.58 nm PBT reflection and the composite 0.35 nm reflection. The 0.35 nm composite reflection gives an average crystallite size of 2.6 nm compared to the 5.6 nm crystallite size in pure PBT fiber. These facts indicate that the crystallite size for PBT is much smaller in the blend fiber than in the pure PBT fiber. This small crystallite size is a result of the processing conditions. There is no large-scale phase separation in the $C < C_{cr}$

solution prior to fiber spinning. After spinning large-scale phase separation of PBT from ABPBI is inhibited by rapid water coagulation of the spun fiber. The orientation of both PBT and ABPBI molecules after spinning is preserved by coagulation. The orientation is further enhanced by some additional drawing of the coagulated fiber in water and later during heat treatment.

Although orientation of both PBT and ABPBI crystallites is relatively high, the fine dispersion of the PBT molecules throughout the matrix material in the fiber prevents PBT from phase separating to form large crystallites. The presence of the small crystallites indicates that a molecular composite has been produced since phase separation of the reinforcing PBT molecules has not occurred at a scale larger than the 30 nm crystallites present in the fiber. A substantial fraction of the PBT molecules may actually be dispersed at a finer scale down to individual molecules, but cannot be detected by WAXD or TEM. If bundles of PBT molecules are no larger than 3 nm in diameter than this reinforcing phase has the high aspect ratio required for efficient reinforcement of the matrix material.

The effect of heat treatment on the $C < C_{cr}$ fiber can also be considered. A comparison of the equatorial diffractometer scans for as-spun (before heat treatment) and heat-treated $C < C_{cr}$ fibers is shown in Figure 16. In the as-spun 30% PBT/70% ABPBI pattern, all peaks present can be indexed to peaks in the as-spun ABPBI fiber. A peak corresponding to a spacing of 0.58 nm, present in PBT, is not present in the 30% PBT/70% ABPBI pattern for the as-spun fiber. This suggests that there are crystallites of ABPBI but not PBT in the as-spun 30% PBT/70% ABPBI fiber. Upon heat treatment, a small additional peak appears in the 30% PBT/70% ABPBI $C < C_{cr}$ fiber pattern with a spacing of 0.62 nm. This spacing corresponds to the 0.58 nm spacing in pure PBT fiber. The emergence of the 0.62 nm peak of the molecular composite can be interpreted as arising either from the formation of small PBT crystallites during heat treatment, or from ordering of larger disordered regions of PBT molecules.

The WAXD pattern of 30% PBT/70% ABPBI $C < C_{cr}$ film is shown in Figure 15. The pattern contains numerous rings, some of which are diffuse and others of which are relatively sharp. The d-spacings for the reflections are listed in Table 4. There is a diffuse 0.74 nm reflection present which is characteristic of an equatorial reflection of pure ABPBI fiber. This indicates that, like the blend fiber, there

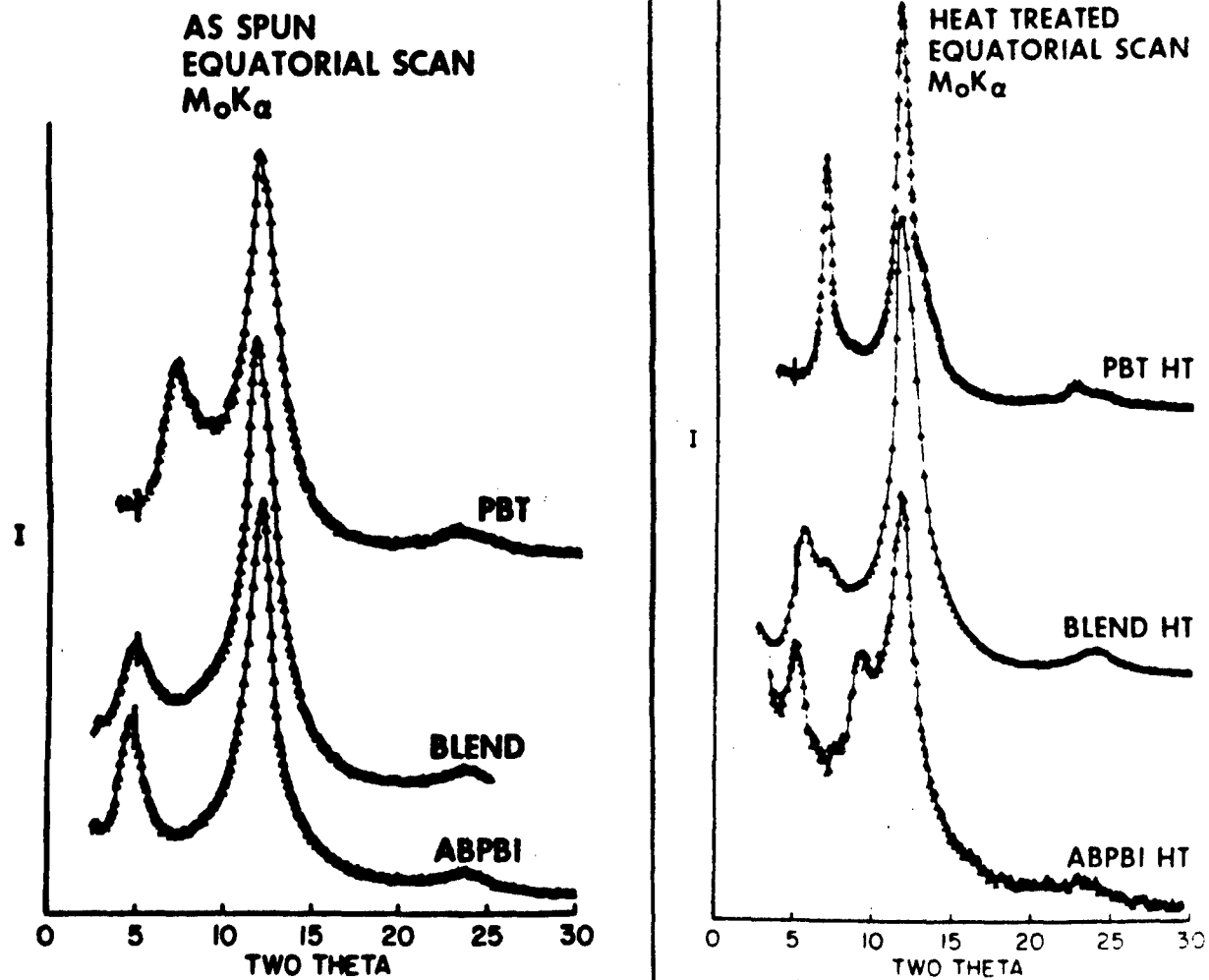


Figure 16., WAXD Equatorial Scans of As-spun and Heat-Treated PBT, ABPBI, and 30% PBT/70% ABPBI $C < C_{cr}$ Fiber

are also small crystallites of ABPBI present in the 30% PBT/70% ABPBI $C < C_{cr}$ film. The lack of arcing in the 0.74 nm ring indicates there is no large scale orientation present. Unlike the blend fiber, there are no spacings present in the blend film characteristic of meridional spacings in the pure ABPBI fiber. This indicates that the lack of shear deformation gradients required for orientation during processing of the blend film has prevented ordering of the ABPBI molecules, even in the presence of the PBT molecules. Thus, it is necessary for orientation to occur during processing to achieve the enhanced ordering of the ABPBI molecules by entanglement and epitaxy with the PBT molecules.

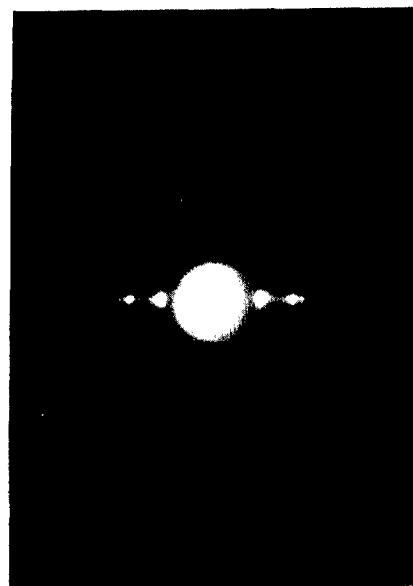
The 0.60 nm spacing present in the 30% PBT/70% ABPBI $C < C_{cr}$ film is characteristic of an equatorial reflection in pure PBT fiber which indicates PBT crystallites are present. Additionally, there are three spacings present (1.25 nm, 0.42 nm, and 0.25 nm) which are characteristic of meridional spacings in the pure PBT fiber. The diffuseness of the 0.60 nm ring indicates the lateral dimensions of PBT crystallites in the blend film are much smaller than those in the PBT fiber, and are probably similar in size, about 2 to 3 nm, to the PBT crystallites in the 30% PBT/70% ABPBI $C < C_{cr}$ fiber. The ring pattern indicates that there is no large-scale orientation of the PBT crystallites. The rings with d-spacings characteristic of pure PBT meridional reflections are relatively sharp. This indicates that the structure along the molecular axis of the PBT molecules in the blend film is well-ordered as would be expected for rigid-rod molecules. The small crystallites indicate phase separation of PBT molecules has probably not occurred at a level greater than about 2 to 3 nm. Thus, a molecular composite is also produced in the 30% PBT/70% ABPBI $C < C_{cr}$ film since the PBT molecules are well-ordered and do not phase separate at a large scale. However, in contrast to the morphology of the "molecular composite" 30% PBT/70% ABPBI fiber, there is no large scale orientation of molecules or crystallites in the "molecular composite" film.

3. TRANSMISSION ELECTRON MICROSCOPY IMAGING AND DIFFRACTION

Dark field images and associated SAED patterns for all samples are shown in Figures 17 to 22. The d-spacings of reflections on the SAED photographs have been measured and are listed in Table 6. The crystallite sizes which have been measured from dark field images are listed in Table 7.

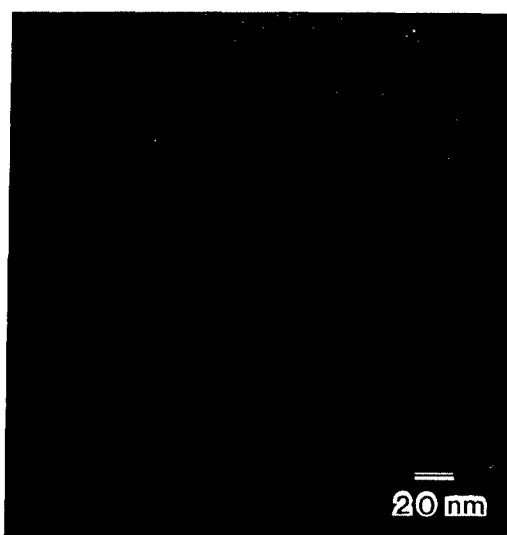


(a)

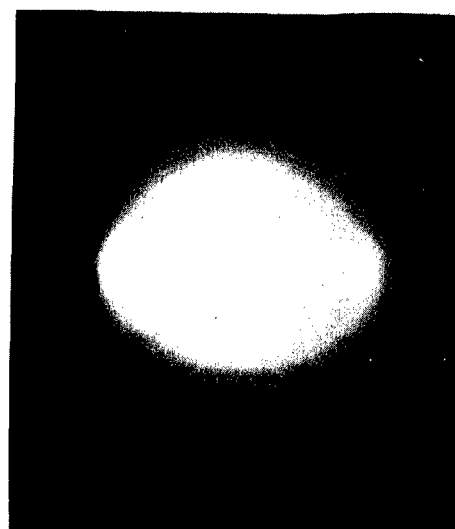


(b)

Figure 17. TEM of PBT Fiber (a) Dark Field Image (b) SAED Pattern

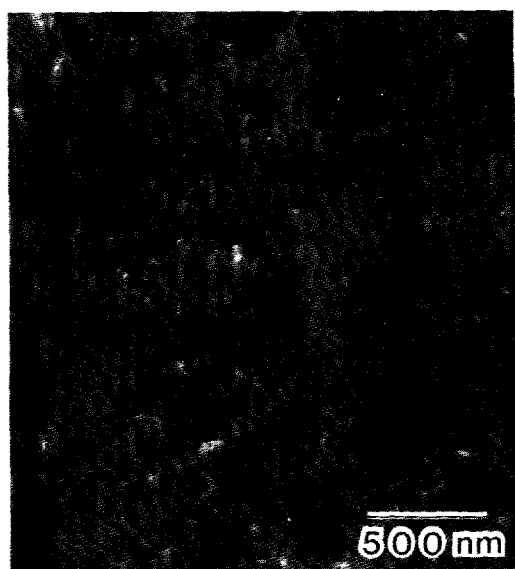


(a)



(b)

Figure 18. TEM of ABPBI Fiber (a) Dark Field Image (b) SAED Pattern

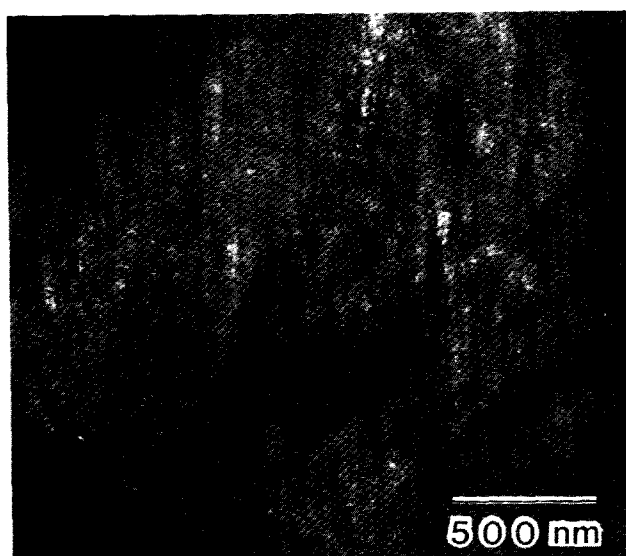


(a)



(b)

Figure 19. TEM of 30% PBT/70% ABPBI $C > C_{cr}$ Fiber (a) Dark Image
(b) SAED Pattern

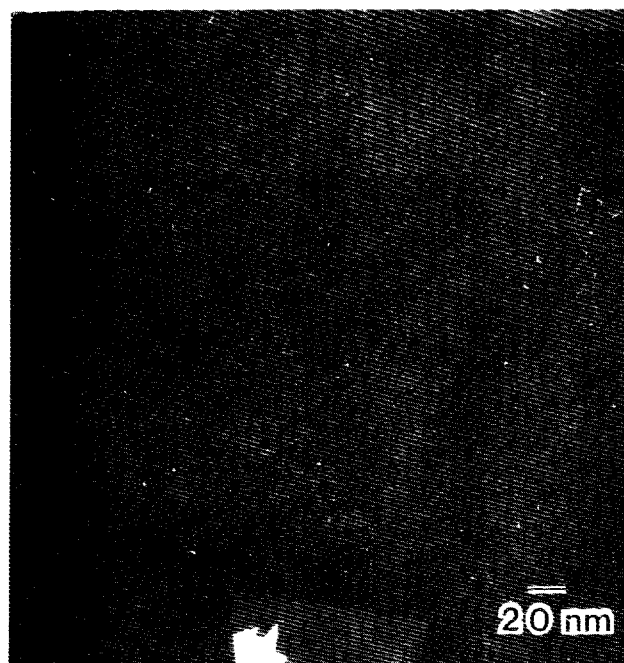


(a)

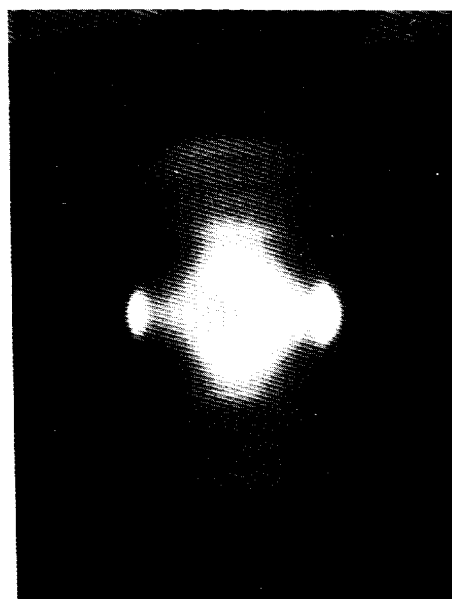


(b)

Figure 20. TEM of 30% PBT/70% ABPBI $C > C_{cr}$ Film (a) Dark Field Image
(b) SAED Pattern

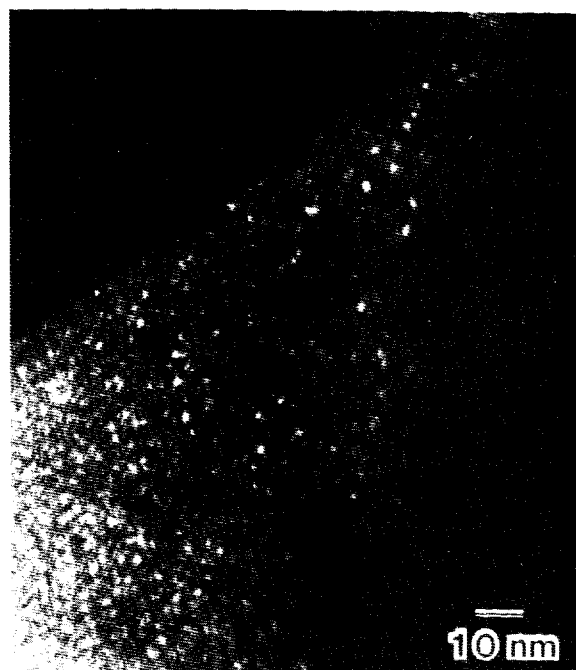


(a)

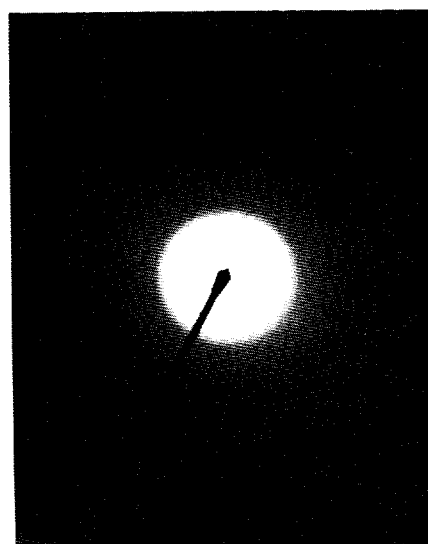


(b)

Figure 21. TEM of 30% PBT/70% ABPBI C_{cr} Fiber (a) Dark Field Image
(b) SAED Pattern



(a)



(b)

Figure 22. TEM of 30% PBT/70% ABPBI C_{cr} Film (a) Dark Field Image
(b) SAED Pattern

TABLE 6. THE D-SPACINGS FOR PBT, ABPBI, AND 30% PBT/70% ABPBI FIBER AND FILM FROM TEM SAED PATTERNS

	PBT	ABPBI	----- 30% PBT/70% ABPBI -----			
	<u>fiber</u>	<u>fiber</u>	<u>C>Ccr</u>	<u>C>Ccr</u>	<u>C<Ccr</u>	<u>C<Ccr</u>
			<u>fiber</u>	<u>film</u>	<u>fiber</u>	<u>film</u>
Equatorial (hk0)	--	.730	--	--	.798	--
d-spacings (nm)	.582	--	.582	.582	--	--
	--	--	--	--	--	--
	.355	.358	.351	.358	.353	.358
	.316	--	--	--	--	--
	.293	--	--	--	--	--
Meridional (00l)	1.25	--	--	1.25	--	--
d-spacings (nm)	--	(.17)	--	--	--	--
	(.63)	--	--	--	--	--
	--	.567	--	--	.577	--
	.415	--	--	.412	.415	.402
	--	(.390)	--	--	.386	--
	.310	--	--	.307	--	.310
	--	(.293)	--	--	.293	--
	.248	--	--	.249	.251	.243
	--	(.234)	--	--	.232	--
	.207	--	.207	--	.209	.206
	--	.199	--	--	.196	--
	.178	--	--	--	--	--
	--	(.167)	.168	--	--	--
	.156	--	--	.157	--	--
	--	(.146)	--	--	--	--
	.138	--	--	.139	--	--
	--	(.130)	--	--	--	--
	.124	--	.124	.123	.128	--
	--	(.117)	--	--	.115	--
	.110	--	--	--	--	.111
	--	.107	--	--	--	--
	.103	--	--	--	--	--
	--	(.098)	--	--	--	--
	.072	--	--	--	--	--

*Parentheses () indicate calculated, not observed values.

TABLE 7. AVERAGE LATERAL CRYSTALLITE SIZE FOR PBT, ABPBI, AND 30% PBT/70% ABPBI FIBER AND FILM FROM TEM DARK FIELD IMAGES

	PBT	ABPBI	----- 30% PBT/70% ABPBI -----			
	<u>fiber</u>	<u>fiber</u>	<u>C>Ccr</u>	<u>C>Ccr</u>	<u>C<Ccr</u>	<u>C<Ccr</u>
			<u>fiber</u>	<u>film</u>	<u>fiber</u>	<u>film</u>
Crystallite Size (nm)	9.5	<3.0	5.0	8.0	<3.0	<3.0

a. PBT Fiber

A typical heat-treated PBT fiber dark field image is shown in Figure 17a. Large coherently diffracting regions about 20 nm long by 10 nm wide are aligned along the fiber axis throughout the fiber. The equatorial ($hk0$) reflections of the diffraction pattern were used for dark field imaging. The presence of only the equatorial reflections of crystallites indicates they are only laterally 2-D ordered. The presence of off-axis (hkl) reflections would indicate axial ordering and overall 3-D ordering, but no off-axis reflections were observed for SAED of PBT or any other samples studied in this report. The coherently diffracting regions are therefore representative of regions with only 2-D lateral ordering. Kink bands, due to compressive buckling along the fiber axis, were often observed in the dark field images.

The PBT fiber SAED pattern is shown in Figure 17b. The features are generally similar to those observed in the WAXD photographs. There are flat, meridional (00ℓ) streaks extending out to 17 orders (the higher orders are distinguishable on the negative, but are too faint to appear on prints). This indicates a high degree of molecular orientation, higher even than found from WAXD. The sharp equatorial ($hk0$) arcing indicates that the crystallites are highly oriented with respect to the fiber axis. The PBT fiber shows a narrower breadth for equatorial reflections than for the other samples discussed later. This narrower breadth is indicative of larger crystallites and/or a higher degree of crystallite perfection in a sample.

In contrast to the WAXD photographs, both the sharpness and the relative intensities of the equatorial reflections varied moderately in SAED patterns from region to region along the length of the PBT fiber and with all other samples studied in this report. This is a texturing effect which occurs along the fiber and is caused by changes in orientation, perhaps due to twisting fibrils. This sometimes occurs in SAED since relatively small volumes are studied in comparison with WAXD (Reference 7). It is concluded that PBT contains highly oriented crystallites with dimensions on the order of 20 nm long by 10 nm wide. The results of the PBT morphology presented here are generally in agreement with the results of earlier studies by Thomas et al (References 2,7).

b. ABPBI Fiber

The dark field image of (hk0) reflections of heat-treated ABPBI fiber shown in Figure 18a shows no large crystallites. Care must be used when interpreting polymer images at this level of resolution because statistical image artifacts ("speckle") are present, especially in thicker areas of the sample (Reference 21). Thus, from considerations of the statistical resolution of the image, any crystallites present would have to be 3 nm or less in size.

The SAED pattern of ABPBI fiber is shown in Figure 18b. The results differ somewhat from those of WAXD photographs. This is probably due to the fact that only the surface of the fiber is examined with detachment replication samples used in TEM SAED. The pattern, like the WAXD photographs, shows sharply-arc'd (hk0) reflections indicating good alignment of the crystallites with the draw axis. The (00 ℓ) meridional reflections extend to six orders and show some slight curvature. These features indicate the molecular orientation with the fiber axis is somewhat less in the ABPBI fiber than in the PBT fiber. The equatorial reflections are broader than those of the PBT fiber, indicating that ABPBI crystallites have smaller lateral dimensions and/or a lower degree of perfection than PBT crystallites. Unlike the WAXD photographs, no (hk ℓ) reflections are visible, which indicates that 3-D order is not present. The discrepancy could again be due to the fact that TEM results are obtained from near the surface of the fiber because of the detachment replication process compared to WAXD which samples the structure of specimens throughout the entire fiber. Also, it may be that the crystallites are too small or the 3-D regions are not prevalent enough to produce observable (hk ℓ) reflections from the areas examined in SAED. A final possibility is that shearing of the ordered liquid crystal phase at the spinneret die walls causes axial disordering of the molecules which prevents the formation of 3-D crystallites at the surface of the fibers. From the above results, it is concluded that the surface TEM samples of the ABPBI fiber contain some moderately well-oriented crystallites which are 2-D ordered, and are no larger than 3 nm in size.

c. 30% PBT/70% ABPBI C>C_{cr} Fiber and Film

The dark field image shown in Figure 19a is from a fiber sample which was spun from C>C_{cr} solution, drawn, and then oven dried. It was prepared for TEM by ultramicrotomy. Elliptical rips and voids appear in the sample, sometimes near

individual particles which are about 0.5 μm in size. Previous SEM results on phase-separated vacuum cast films indicated that such particles are phase-separated aggregates composed chiefly of PBT. The rips and voids are due to the shearing of the hard, phase-separated PBT rich aggregates through the softer ABPBI rich matrix material during ultramicrotomy. The dark field image shows crystallites within the phase-separated aggregates with sizes on the order of 10 nm.

The SAED pattern from the fiber is shown in Figure 19b. There are a total of five slightly arced reflections present. The first, more intense, but somewhat diffuse reflection has d-spacing of 0.58 nm which indicates that small PBT crystallites are present. The second more intense and diffuse reflection has a d-spacing of 0.35 nm and is characteristic of both PBT and ABPBI crystallites. However, since this is a composite reflection it is not possible to unambiguously identify the presence of ABPBI crystallites. There are three slightly sharper reflections present at .207 nm, .168 nm, and .124 nm. These are characteristic PBT meridional reflections. Their presence indicates that the PBT molecules have retained their order in this sample.

Figure 20a is a dark field image of a particle from a film which was vacuum cast from $C > C_{cr}$ solution. The sample was prepared for TEM by ion thinning. Crystallites within the particle have sizes on the order of 10 nm. The particles are about 4 to 6 times larger in the phase-separated film than in the fiber. This is because in fiber spinning, the fiber is sheared, which causes large domains to break up and form the smaller particles. During the vacuum casting process, the molecules have more time to diffuse in the quiescent, increasingly concentrated solution, enhancing phase separation. This results in the larger aggregates observed in the vacuum cast film. It also appears that the crystallites, which have aggregated together to form the particle, are larger in size than crystallites in the fiber. Quiescent crystallization may be more effective in forming larger crystallite than the shear and elongational flow processes in fiber spinning.

A typical SAED pattern from within an aggregate in the phase-separated film is shown in Figure 20b. The pattern contains relatively sharp and moderately well-arced equatorial reflections, indicating that there are large, moderately well-oriented crystallites within the aggregates. Several orders of fairly sharp, but

slightly curved, meridional reflections are present, indicating moderate molecular orientation. By using the meridional (001) spacing of PBT, which does not vary with processing, as a standard, the d-spacings of the equatorial reflections can be calculated. These are listed in Table 6. The presence of the 0.60 nm reflection indicates that PBT crystallites are present. This agrees with the SEM observations and backscattering results which showed that the aggregates are brittle and indicated that they are probably composed chiefly of PBT. Additionally, it has been found from the diffraction pattern that the longitudinal axis of the PBT molecules and crystallites are aligned with the longitudinal axis of the aggregate particles. This is in agreement with earlier findings from the SEM studies.

From the above results, it is concluded that both 30% PBT/70% ABPBI $C > C_{cr}$ fiber and film contain phase-separated aggregates within a ductile matrix. These aggregates are chiefly composed of moderately oriented 8 to 10 nm wide PBT crystallites.

d. 30% PBT/70% ABPBI $C < C_{cr}$ Fiber and Film

The TEM dark field image from the (hk0) reflections of the fiber spun from 30% PBT/70% ABPBI $C < C_{cr}$ solution is shown in Figure 21a. There are no obviously discernible features greater than 3 nm in size. From this observation and limitations of the statistical resolution of the image, it can be concluded that the size of any crystallites that are present would have to be about 3 nm or less.

Figure 21b shows the SAED pattern for $C < C_{cr}$ fiber. It contains a broad moderately well-arc'd equatorial reflection at 0.853 nm. This indicates that ABPBI crystallites are present, but that they are very small and/or disordered. This is in agreement with the dark field results. The 0.35 nm reflection is a composite reflection for PBT and ABPBI structures. It indicates that PBT and/or ABPBI crystallites may be present. The moderate arcing of the equatorial reflections indicates moderate crystallite orientation along the fiber axis. The previous SAED results are supported by WAXD results which also indicate the presence of small and/or disordered crystallites which are moderately-oriented. The broad and somewhat curved meridional reflections indicate that there is also good orientation of the molecules with respect to the fiber axis. The presence of three meridional orders characteristic of ABPBI meridional reflections indicates that the ABPBI

molecules are well enough oriented and ordered to produce meridional reflections. Although the diffuseness of the pattern makes measurement of spacing difficult, there are clearly two distinct sets of meridional spacings present. Measurement of the spacings indicate that ordered molecules of both PBT and ABPBI are present.

The film studied was prepared by spinning from $C < C_{cr}$ solution, with subsequent neutralization and heat treatment. The dark field image of 30% PBT/70% ABPBI $C < C_{cr}$ film in Figure 22a shows diffracting regions no larger than 3 nm in size present at the thinnest edges of the film. These regions are probably crystallites since WAXD indicated a presence of small crystallites, although statistical "speckle" (as discussed earlier) is a possibility. Other inhomogeneties larger than 3 nm are not observed.

The SAED photographs for the film is shown in Figure 22b. There are both diffuse and sharp rings present. The rings indicate that the crystallites and molecules are unoriented. The diffuse reflection occurs at .384 nm and is characteristic of both PBT and ABPBI crystallites. Since this is the only equatorial reflection present it is not possible to determine whether PBT or ABPBI or both types of crystallites are present. The remaining reflections, which are all relatively sharp, are characteristic of the meridional spacings of PBT. This indicates that PBT molecules are well ordered in this film.

It is concluded from the dark field images and SAED patterns that 30% PBT/70% ABPBI $C < C_{cr}$ fiber contains small, moderately well oriented crystallites of PBT and ABPBI which are no larger than 3 nm in diameter. The crystallites in the film are very small and are unoriented. The TEM images show that no crystalline phase separation occurs at a scale larger than 3 nm for either the fiber or the film. The PBT and ABPBI components have been dispersed at a scale finer than 3 nm. Thus, a molecular level composite has been formed in both the fiber and the film.

4. ANALYTICAL ELECTRON MICROSCOPY

a. Energy Dispersive X-ray Analysis

EDS has been used to study the composition of phase-separated fiber. Figure 23 contains two spectra from a bulk sample of the phase-separated fiber obtained with EDS on a SEM. Figure 23a is a spectrum from a particle, while Figure

23b is a spectrum from the matrix. The spectra were obtained under identical conditions. The copper peaks are background from the sample holder. Sulfur is the only element in the polymers with an atomic number high enough (>10) to be detected. The sulfur peak is much larger in the aggregate spectrum than in the matrix spectrum. Since PBT contains sulfur while ABPBI does not, this indicates that PBT is much more concentrated in the aggregates than in the matrix. Even though this spectrum of the matrix shows sulfur present, this does not necessarily indicate the presence of PBT in the matrix of an amount equivalent to the relative peak heights. This is because the electrons from the beam can spread out more than a micron in the sample and cause X-rays to be emitted from nearby particles. Also, there may be a small contribution from residual solvent (MSA), since studies on similar polymers show that about 1% of solvent remains in processed fibers (Reference 22).

Figure 24 is an EDS x-ray elemental map of the phase-separated film using the sulfur peak in EDS by STEM. The particles appear as ellipsoidal regions in the underlying image. Although the background is rather high, it is evident that more sulfur x-ray counts (bright dots) appear in the particles than in the matrix. This indicates a higher concentration of sulfur, and thus PBT, in the particles than in the matrix. This is in agreement with the above EDS spectra and also with earlier SEM backscattering results.

b. Electron Energy Loss Spectroscopy

Figure 25a is the EELS spectrum obtained from a particle in the phase-separated film. The most prominent edge in the spectrum is the carbon K edge. The smaller peak is the sulfur L edge. A nitrogen peak does not appear even though PBT contains 11 weight percent nitrogen. The elemental detection limit for EELS is stated to be usually on the order of one weight percent. However, this value is obtained under the idealized conditions of maximum beam intensity and very thin samples. With polymeric materials, the beam intensity is necessarily low to prevent beam damage, and it is difficult to limit the thickness of the sample. These factors contribute to a high background in the EELS spectra. Thus, it is not unreasonable for the nitrogen edge of PBT to be masked by the background.

Figure 25b is the EELS spectrum from the matrix region of the sample. The sulfur edge is not present above background. A small nitrogen K edge appears after

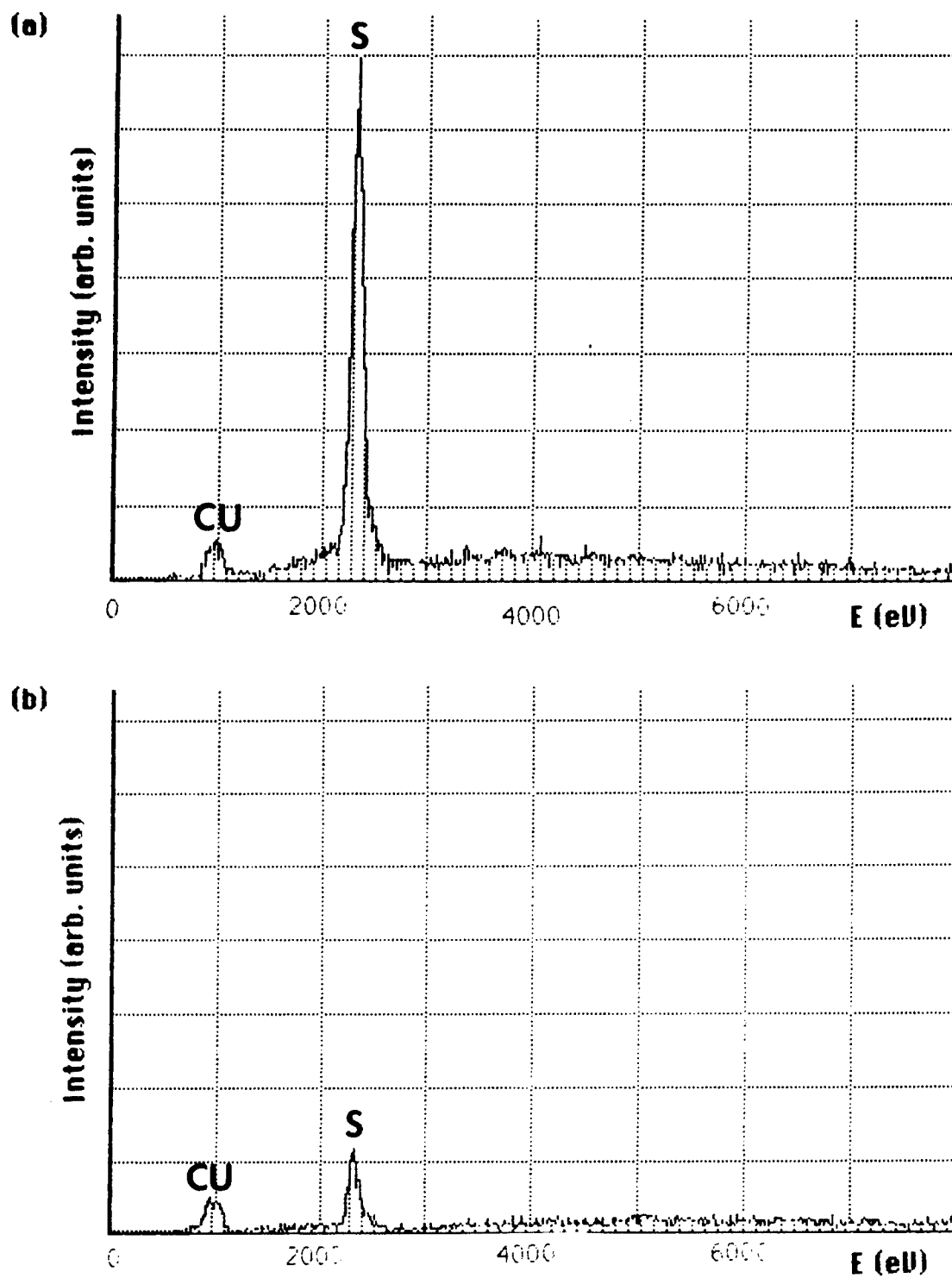


Figure 23. Energy Dispersive X-ray Spectra from 30% PBT/70% ABPBI $C > C_{cr}$ Fiber



Figure 24. Sulfur X-ray Map of 30% PBT/70% ABPBI C>C_{cr} Film

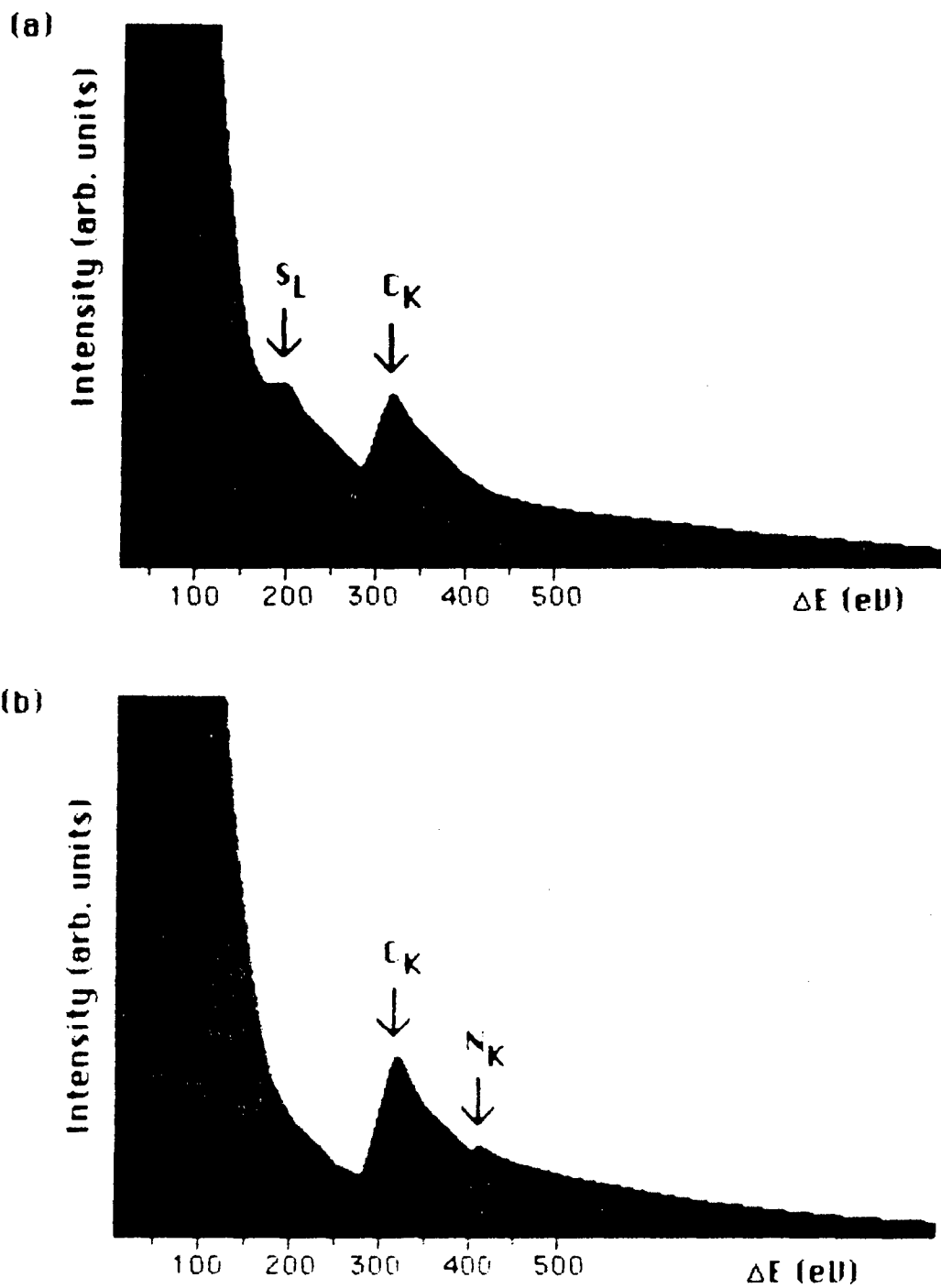


Figure 25. Electron Energy Loss Spectra from 30% PBT/70% ABPBI $C > C_{cr}$ Film

the carbon edge. This is because ABPBI contains 24 weight percent nitrogen compared to the 11 weight percent nitrogen for PBT. These results indicate that the particles have significantly larger amount of PBT than the matrix while the matrix has a significantly larger amount of ABPBI than the particles. This is in agreement with the previously discussed results of SEM imaging, TEM dark field imaging, and SAED.

c. Microdiffraction

Figure 26 is a microdiffraction pattern from a particle in the $C > C_{cr}$ film. The equatorial reflections are fairly well-arc'd and have a moderate breadth. The meridional reflections are faint but are also well-arc'd with a moderate breadth. This indicates that molecules and crystallites within the aggregate are fairly well-oriented and that the crystallites have a moderate size. The d-spacings indicates the crystallites are PBT. These results are in agreement with earlier SAED results.

5. GENERAL DISCUSSION

The PBT fiber SEM images show that the fiber has little ductility, in agreement with stress-strain curves which show linear elastic behavior to the fracture point (Reference 4). WAXD patterns and TEM dark field images showed that pure PBT heat-treated fiber contained crystallites which were about 10 nm wide laterally. TEM showed that these regions were extended to about 200 nm in length. WAXD and SAED patterns showed the crystallites and molecules of PBT were highly oriented. WAXD showed the orientation of the molecules was higher parallel to the plane of the heterocyclic rings.

In the ABPBI SEM images, the presence of drawing and micronecking is in agreement with mechanical testing results which showed that ABPBI fiber had higher ductility (5.2%) and lower strength (1090 MPa) when compared with values measured for PBT (1.1% and 2800 MPa, respectively). TEM dark field images showed that ABPBI heat-treated fiber crystallites are no larger than 3 nm in size, in agreement with WAXD measurements which showed the presence of 3.2 nm crystallites. SAED patterns and WAXD measurements showed these crystallites are not as highly oriented as those in PBT fiber. WAXD patterns showed that ABPBI crystallites in the fiber are three-dimensionally ordered, while the TEM showed that crystallites at the surface of the fiber are only 2-D ordered. The 3-D ordering and higher orientation contribute to higher ductility and lower fibrillation compared to the PBT fiber.

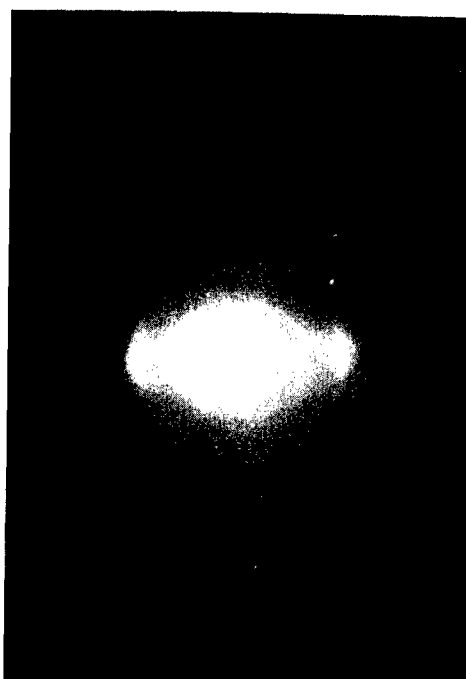


Figure 26. Microdiffraction Pattern from a Particle in 30% PBT/70% ABPBI
 $C > C_{cr}$ Film

When fiber and film are processed from 30% PBT/70% ABPBI $C > C_{cr}$ solution, SEM and TEM images show phase separation occurs and micron-scale particles are formed. TEM reveals that these phase-separated aggregates are composed of crystallites which are about 8 to 10 nm in size, and SAED indicates the crystallites and molecules are moderately oriented with the longitudinal axis of a particle.

There are a variety of observations which lead to the conclusion that the crystallites in the particles are PBT crystallites. First, both SAED and AEM micro-diffraction patterns reveal crystallites of PBT present in the particles. In addition, the EDS results show that the concentration of PBT is much higher in the particles than in the matrix of the phase-separated material. The EELS spectra also show the PBT to be located chiefly in the particles and not in the matrix. The brittleness of the particles, as shown in SEM images, also indicates the particles are chiefly PBT. Finally, ABPBI crystallites in pure ABPBI fiber and film have been observed to be much smaller than the 10 nm crystallites observed in the aggregates. The conclusion that the aggregates contain chiefly PBT is supported by earlier SEM backscattering work. Thus, it is unlikely that there are crystallites of ABPBI present within the particles. It may, however, be possible that some ABPBI exists within the particles as a non-crystalline material. However, this is contrary to Flory's prediction of total exclusion of flexible coil molecules from the rigid rod phase (References 23, 24). Phase separation of the PBT molecules would be expected due to their rigid-rod geometry, which creates a tendency for the PBT molecules to pack laterally. This tendency will promote phase separation of the PBT into particles.

Since there is less PBT than ABPBI in the total sample (30% PBT/70% ABPBI), relatively little PBT would be left in the matrix material if the aggregates are mostly PBT. The matrix of the phase-separated fiber showed some ductility in SEM photographs similar to the ductility observed in SEM photographs of fractured ABPBI fibers. This is probably due both to the reduced amount of PBT in the matrix and the overall reduced orientation in these samples. EDS spectra from the matrix show only a small sulfur peak, which limits the maximum amount of PBT in the matrix to a small value. EELS results, which have worse statistics than EDS results, show the presence of a nitrogen peak, but not a sulfur peak, in the matrix material, indicating a relatively large amount of ABPBI in the matrix material. Thus, these

data indicate the matrix is chiefly ABPBI. This is in agreement with Flory's theory which predicts some, but little, rigid-rod polymer will still be present in the coil phase. The mechanical properties of the phase separated materials are also rather low because of the low aspect ratio of about four of the particles and also the poor adhesion of the particles to the matrix. These factors result in inefficient reinforcement of the matrix material by the PBT in particles. Additionally, lower orientation in the phase-separated fibers compared to the "molecular composite" fibers would also result in lower values of mechanical properties.

When fiber and film are processed from 30% PBT/70% ABPBI solution, so that the total concentration of polymer solids is kept below C_{cr} , no large-scale phase separation is observed. The SAED and WAXD patterns indicate that both PBT and ABPBI crystallites are present. TEM dark field images reveal no features present at a scale larger than 3 nm. This demonstrates that a dispersion of PBT in ABPBI at a molecular level of 3 nm or better has been achieved. Stated more conservatively, it can be said that no crystalline phase separation occurs at a scale larger than 3 nm. A polymer blend with this level of dispersion is considered to be a molecular composite. Crystallites or bundles of PBT less than 3 nm in lateral size may be present in the molecular composite, but this cannot be determined from TEM. Thus, the aspect ratio of the reinforcing phase of PBT molecules and molecular bundles is very high in the molecular composite fiber and film compared to the PBT in particles in the phase-separated fiber and film. This results in more efficient reinforcement of the matrix. In the molecular composite film, the values of strength and modulus are, respectively, 8 and 26 times greater than those of the phase-separated film. In the molecular composite fiber, SAED patterns show that the PBT and ABPBI molecules and crystallites are also moderately well-oriented. Both the efficient reinforcement and the enhanced orientation of ABPBI by PBT results in high values of mechanical properties in the molecular composite fiber. The values of its strength and modulus are, respectively, 7 and 11 times greater than those of the phase-separated fiber. In a comparison of the mechanical properties of the highly oriented molecular composite fiber to the almost unoriented molecular composite film, both the strength and modulus are only about 25% higher in the fiber. The differences in the magnitude of the effects of phase separation and orientation on mechanical properties suggests that the level of molecular dispersion may have a much greater effect on strength and modulus than does molecular orientation.

The values of elongation to break for the molecular composite fiber and film are considerably reduced compared to those for the phase-separated fiber and film. The value for elongation to break is about nine times higher for the phase-separated fiber compared to the molecular composite fiber, and about two times higher for the phase-separated film compared to the molecular composite film. This occurs because the reinforcing PBT has phase separated out of the matrix material in the phase-separated fiber and film, thus giving the matrix material a larger fraction of the more ductile ABPBI. In the phase-separated fiber there is only limited orientation compared to the highly oriented molecular composite film. The higher orientation of molecules in the molecular composite fiber limits the amount of elongation prior to fracture. In a comparison of the mechanical properties of the highly oriented molecular composite fiber to the almost unoriented molecular composite film, the value for elongation to break is only about 70% higher in the film. Again, the higher orientation of the molecular composite fiber limits the amount of elongation prior to fracture. The above comparisons suggest that ductility, like strength and modulus, may be more affected by the level of molecular dispersion than by molecular orientation.

SECTION IV

SUMMARY AND CONCLUSIONS

SEM, TEM, and WAXD were used to examine the structure and morphology of fiber and film of PBT and ABPBI homopolymers and a 30% PBT/70% ABPBI blend. AEM was used to study the composition and structure of phase-separated 30% PBT/70% ABPBI film and fiber.

Heat-treated PBT homopolymer fiber contained 20 nm long by 10 nm wide crystallites which were two-dimensionally ordered. The molecules and crystallites in these fibers were highly oriented with respect to the fiber axis. The a-axis of crystallites was more highly oriented (-.46) than the b-axis (-.41) indicating that slip along molecules in the liquid crystal state was easier between planes of the heterocyclic rings than perpendicular to those planes. High molecular and crystallite orientation contributed to high strength and modulus and low ductility of the fiber.

Heat-treated ABPBI homopolymer fiber contained crystallites which had lateral dimensions no larger than 3 nm. The crystallites were three-dimensionally ordered within the fiber, but only two-dimensionally ordered at the fiber surface. Crystallites and molecules were moderately well-oriented with respect to the fiber axis. The higher orientation of the a-axis (-.43) compared to the b-axis (-.38) indicated that, like PBT, slip along molecules in the liquid crystal state was easier between planes of the heterocyclic rings than perpendicular to those planes. The 3-D ordering and lower orientation contributed to lower strength and modulus and higher ductility of the ABPBI fiber when compared to the PBT fiber.

A 30% PBT/70% ABPBI blend processed from a $C > C_{cr}$ solution into oven-dried fibers and films contained brittle, 0.1 to 4 micron long ellipsoidal particles which were phase separated from the surrounding matrix material. Phase separated particles were 10 to 20 times larger in the vacuum cast film compared to the wet spun fiber. The particles were composed chiefly of an agglomeration of 8 to 10 nm PBT crystallites with the PBT c-axis moderately well-aligned with respect to the longitudinal axis of a particle. The matrix material was ductile and composed chiefly of ABPBI. Low values of strength and modulus in the fibers and films were due to phase separation of the PBT molecules from the matrix material, lack of high

molecular and crystallite orientation, and also the low temperature of heat treatment.

Heat-treated fiber and film processed from an optically homogeneous $C < C_{cr}$ 30% PBT/70% ABPBI solution exhibited no large scale phase separation. Phase separation was inhibited by rapid water coagulation of fiber and film during the spinning or extrusion process. The fiber and film contained two-dimensionally order crystallites of both PBT and ABPBI with lateral dimensions no larger than 3 nm. The molecules and crystallites were well-oriented in the fiber and almost unoriented in the film. It was concluded that the PBT in the fiber and film was dispersed at the molecular level in the ABPBI at a scale no larger than 3 nm, resulting in a molecular composite. In the molecular composite film, the fine dispersion of the rigid-rod PBT molecules efficiently reinforced the matrix material. The values of its strength and modulus were, respectively, 8 and 26 times greater than those of the phase separated film. In the molecular composite fiber, efficient reinforcement and enhanced orientation of ABPBI by PBT resulted values of strength and modulus which were, respectively, 7 and 11 times greater than those of the phase separated fiber. In comparison of the mechanical properties of the highly oriented molecular composite fiber to the virtually unoriented molecular composite film, both the strength and modulus were only about 25% higher in the fiber. The differences in the magnitude of the effects of phase separation versus orientation on mechanical properties suggest that the level of molecular dispersion may have a much greater effect on strength and modulus than does molecular orientation.

We believe that the results presented here conclusively demonstrate the achievement of a molecular composite using rigid-rod molecules to form a high-aspect ratio reinforcement for a ductile polymer matrix. However, this conclusion is based upon data from characterization techniques which require structure to be periodically ordered. It is also possible for phase separation to occur in the form of disordered or amorphous phases. If this were to occur, the techniques used in this paper may not be sufficiently sensitive to detect disordered or amorphous domains. We are pursuing this problem in conjunction with other laboratories by applying other techniques such as solid-state nuclear magnetic resonance spectroscopy and excimer fluorescence spectroscopy. Verification of the degree of dispersion of the rod-like polymer is an essential step in the understanding and realization of the full potential of the properties of molecular composites.

REFERENCES

1. T. E. Helminiak, Amer. Chem. Soc. Org. Coatings Plast. Prep. 40 (1979) 475.
2. E. L. Thomas, R. J. Farris, S. L. Hsu, S. Allen, A. Filippov, J. Minter, E. Roche, K. Shimamura, T. Takahashi, and G. Venkatesh, AFWAL-TR-80-4045, Vol. 2 (1980).
3. J. R. Minter, AFWAL-TR-82-4097 (1982).
4. S. R. Allen, AFWAL-TR-83-4052 (1983).
5. E. J. Roche, T. Takahashi, and E. L. Thomas, ACS Symp. Ser. 141 (1980) 303.
6. J. A. Odell, A. Keller, E. D. T. Atkins, and M. J. Miles, J. Mater. Sci. 16 (1981) 3309.
7. E. L. Thomas, R. J. Farris, and S. L. Hsu, AFWAL-TR-80-4045, Vol. I (1980).
8. K. Shimamura, J. F. Minter, and E. L. Thomas, J. Mater. Sci. Lett. 2 (1983) 54.
9. A. V. Fratini, E. M. Cross, J. O'Brien, and W. W. Adams, AFWAL-TR-85-4097 (1985).
10. A. V. Fratini, University of Dayton, private communication (1985).
11. G. Price, University of Dayton Research Institute Technical Report No. UDRI-TR-80-41 (1980).
12. S. J. Krause and W. W. Adams, Proc. Ann. EMSA Meeting 41 (1983) 32.
13. W-F Hwang, D. R. Wiff, C. L. Benner, and T. E. Helminiak, J. Macromol. Sci - Phys. B22(2) (1983) 231.
14. T. E. Helminiak, U. S. Patent Application 902 525, 1978.
15. G. Husman, T. Helminiak, W. Adams, D. Wiff, and C. Benner, ACS Symp. Ser. 132 (1980) 203.
16. M. Takayanagi, Pure and Appl. Chem. 55 (1983) 819.
17. R. M. Christensen, Mechanics of Composite Materials, John Wiley and Sons, New York, 1979.
18. A. K. Kulshreshtha and G. E. Price, AFWAL-TR-82-4047 (1982).
19. M. Wellman, G. Husman, A. K. Kulshreshtha, T. Helminiak, D. Wiff, C. Benner, and W-F. Hwang, Org. Coat. Plast. Chem. 43 (1980) 783.
20. W-F Hwang, D. R. Wiff, C. Verschoore, G. E. Price, T. E. Helminiak, and W. W. Adams, Polym. Eng. and Sci. 23 (1982) 784.

REFERENCES (Concluded)

21. E. J. Roche and E. L. Thomas, Polymer 22 (1981) 333.
22. W-F. Hwang, University of Dayton, private communication (1983).
23. P. J. Flory, Proc. Roy. Soc. London A234 (1956) 73.
24. P. J. Flory, Macromolecules 11 (1978) 1138.

APPENDIX A

LITERATURE SURVEY ON ELECTRON MICROSCOPY OF POLYMERS

The literature survey in this appendix covers topics related to this report. The references contained herein were obtained by both manual and computer-aided searches. As one goes from the specific topic of this report to closely related topics, one finds the literature sources diversifying quite rapidly. "Electron microscopy of polymers" branches out into the fields of chemistry, physics, and engineering. Hence, no claim is made as to the completeness of the literature survey. However, the survey does indicate the breadth of the subject. References in the main body of the report are described therein and are omitted here.

The survey is divided into three sections: analytical techniques, electron microscopy of specific polymers, and beam damage. The latter section, being the most extensively covered topic of the three, is further subdivided. Within each section, discussion generally starts with either articles very closely related to the report or with basic references and proceeds to more specialized references. Authors' names are in boldface type in the discussion to aid in quick location.

ANALYTICAL TECHNIQUES

This section includes both general discussion of analytical electron microscopy as well as specific applications to polymeric and biological samples. Perhaps the most highly regarded reference in this field is "Introduction to Analytical Electron Microscopy" by J. J. Hren et al. Three articles contained within it are particularly relevant to this report. Zaluzec lists all the precautions necessary while performing x-ray microanalysis, and provides constants and formulas required for quantitative work. One section deals with a material with precipitate phases, analogous to the topic of phase-separation. Maher provides a good "how-to" for EELS data analysis, while Johnson has a very good discussion of EELS applications and limitations for biological (and thus polymeric) samples.

Three other articles provide general references concerning EELS. Williams presents a comprehensive and readable review of EELS uses and limits, both qualitative and quantitative, and also provides an extensive set of references. Joy and Maher discuss the theoretical problem of minimum detectable atoms and mass

fractions of elements in EELS, giving specific examples using derived equations. Egerton provides a computer program to calculate theoretical inelastic cross-sections, thus providing the basis for quantitative EELS.

Egerton and Misra discuss the information obtained from the technique of "Z-contrast" -a method which divides the annular dark field intensity by the inelastic intensity. The effect of sample thickness on the usefulness of this technique for compositional analysis is considered. Engel et al. report on a computerized image acquisition and processing system which is especially useful for enhancing images of biological samples.

The article by White and Thomas is a review describing SEM operation and theory, sample preparation, beam damage, etc., including the use of the analytic features of SEM's and examples of microstructures observed. Sherman and Thomas discuss microdiffraction patterns obtained using STEM with respect to theory. Sherman et al. compare DF images to microarea diffraction patterns obtained on a CTEM with scanning attachments.

Five articles are examples of using certain AEM techniques on specific samples. Johnson calculates optical constants for two nucleic acid bases from their energy loss spectra via dielectric theory. Radiation damage is also considered. Holsworth uses EDS to aid in determining the morphology of latex paints (TiO_2) and acrylic coatings on metal substrates. Briber employs microdiffraction from about a $1 \mu\text{m}^2$ area in a morphological study of certain polyurethanes. Low et al. study polyethylene with STEM, including bright and dark field imaging and microdiffraction; their format of investigation somewhat parallels this report. Chacko et al. describe the techniques of BF "ghost" imaging and STEM annular dark field as applied to polyethylene.

R. M. Briber, "The Identification and Characterization of Two Crystal Forms in MDI/BDO Based Polyurethanes by STEM, TEM, and Microdiffraction", Proc. Ann. EMSA Meeting 40 (1982) 674.

V. P. Chacko, W. W. Adams and E. L. Thomas, "Imaging of Polyethylene Films by Diffraction Contrast", J. Mat. Sci. 18 (1983) 1999.

R. F. Egerton, Ultramicroscopy 4 (1979) 169.

- R. F. Egerton and M. Misra, "Calculations of Z-Contrast for Organic and Biological Specimens", Proc. Ann. EMSA Meeting 41 (1983) 284.
- A. Engel, M. Strahm, B. Michel and J. Dubochet, "An On-Line Data Processing System Suitable for Biological S.T.E.M.", in "Scanning Electron Microscopy/1977/I (Proc. of IIT Workshop on AEM)", edited by O. Johari (Chicago Press, Chicago, 1977), p. 365.
- R. M. Holsworth, "Organic Coatings Analysis by S.E.M. and Energy Dispersive X-Ray Analysis", in "Advances in Chemistry Series, Volume 203: Polymer Characterization", edited by C. D. Craver (American Chemical Society, Washington, 1983) p. 363.
- D. E. Johnson, "Energy Loss Spectrometry for Biological Research", in "Introduction to Analytical Electron Microscopy", edited by J. J. Hren et al. (Plenum Press, New York, 1979) p. 295.
- D. E. Johnson, "The Interactions of 25 keV Electrons with Guanine and Cytosine", Radiation Research 49 (1972) 63.
- D. C. Joy and D. M. Maher, "Electron Energy Loss Spectroscopy: Detectable Limits for Elemental Analysis", Ultramicroscopy 5 (1980) 333.
- A. Low, D. Vesley, P. Allan and M. Bevis, "An Investigation of the Microstructure and Mechanical Properties of High Density Polyethylene Spherulites", J. Mat. Sci. 13 (1978) 711.
- D. H. Maher, "Elemental Analysis Using Inner-Shell Excitations: A Microanalytical Technique for Materials Characterization", in "Introduction to Analytical Electron Microscopy", edited by J. J. Hren et al. (Plenum Press, New York, 1979) p. 259.
- E. S. Sherman and E. L. Thomas, "Scanning Microdiffraction of Polymers", J. Mat. Sci. (14) (1979) 1109.
- E. S. Sherman, W. W. Adams and E. L. Thomas, "Dark Field Imaging of Semicrystalline Polymers by Scanning Transmission Electron Diffraction", J. Mat. Sci. 16 (1981) 1.
- J. R. White and E. L. Thomas, Rubber Chem and Tech. 57 (1984) 457.
- D. B. Williams, "Electron Energy Loss Spectrometry in the Analytical Electron Microscope", Norelco Reporter 30 (1983) 16.
- N. J. Zaluzec, "Quantitative X-Ray Microanalysis: Instrumental Considerations and Applications to Materials Science", in "Introduction to Analytical Electron Microscopy", edited by J. J. Hren et al. (Plenum Press, New York, 1979) p. 121.

Electron Microscopy of Specific Polymers

This section covers general electron microscopy studies of polymers which do not emphasize analytical techniques or beam damage. Two articles investigate PBT. Minter et al. use TEM imaging and diffraction, WAXD, and SAXS to examine the

morphology of heat-treated PBT. Odell et al. use x-ray and electron diffraction results to develop a model of the unit cell and molecular packing of PBT. Kink bands in the closely related polymer PPTA (KevlarTM) are examined by optical microscopy, TEM imaging and diffraction, and WAXD by Takahashi et al.

Composite materials are discussed in five of the articles. Hayashi et al. study a poly(styrene-divinylbenzene)/poly(vinyl chloride) system (abbreviated P(St-DVB)/PVC), and use TEM imaging to show that micron-sized domains of PSt/PVC containing 30 nm regions of PSt are dispersed in a matrix of P(St-DVB). Gupta et al. show dispersed second-phase domains in SEM fracture images of polyethylene - polypropylene composites. Hanchett and Geiss utilize stereoscopic TEM imaging from relatively thick specimens to determine particle dispersion and distribution. Zachariades et al. investigate the morphology of a copolyester with techniques such as TEM imaging and diffraction, and WAXD. Chacko et al. image a composite of CaCO₃ powder in polyethylene to discover crazes.

Polyethylene, the "reference" polymer for beam damage studies, is the main topic of one article. Adams has a series of STEM dark field images of PE during in situ deformation, and obtains the periodicity by optical transform of a TEM bright field image. Both optical and electron microscopy of polymers are briefly overviewed by Hobbs, with emphasis on rubbers and characterization of large-scale morphology.

- W. W. Adams, "Visualization by STEM Annular Dark Field of Intralamellar Shear in Polyethylene", Proc. Ann. EMSA Meeting 41 (1983) 26.
- V. P. Chacko, R. J. Farris and F. E. Karasz, "Tensile Properties of CaCO₃-Filled Polyethylenes", J. Appl. Poly. Sci. 28 (1983) 2701.
- A. K. Gupta, V. B. Gupta, R. H. Peters, W. G. Harland and J. P. Berry, "The Effect of Addition of High-Density Polyethylene on the Crystallization and Mechanical Properties of Polypropylene and Glass-Fiber-Reinforced Polypropylene", J. Appl. Poly. Sci. 27 (1982) 4669.
- V. E. Hanchett and R. H. Geiss, "Electron Microscopy of Carbon-Loaded Polymers", IBM J. Res. Develop. 27 (1983) 348.
- T. Hayashi, J. Ito, K. Mitani and Y. Mizutani, "Dynamic Mechanical Properties and Morphology of Styrene-Divinylene Copolymer/Poly(Vinyl Chloride) Systems", J. Appl. Poly. Sci. 28 (1983) 2867.

- S. Y. Hobbs, "Polymer Microscopy", J. Macromolecular Sci. -Rev. Macromol Chem. C 19,2 (1980) 221.
- J. R. Minter, K. Shimamura and E. L. Thomas, "Microstructural Study of As-Extruded and Heat-Treated Ribbons of Poly(p-Phenylene Benzobisthiazole)", J. Mat. Sci. 16 (1981) 3303.
- J. A. Odell, A. Keller, E. D. T. Atkins and M. J. Miles, "Structural Studies of Poly(p-Phenylene Benzobisthiazole) Films", J. Mat. Sci 16 (1981) 3309.
- T. Takahashi, M. Miura and K. Sakurai, "Deformation Band Studies of Axially Compressed Poly(p-Phenylene Terephthalamide) Fiber", J. Appl. Pol. Sci. 28 (1983) 579.
- A. Zachariades, J. Economy and J. Logan, "The Morphology of the Aromatic Copolyester of Poly(Ethylene Terephthalate) and 80 mol% of P-Acetoxybenzoic Acid", J. Appl. Poly. Sci. 27 (1982) 2009.

Beam Damage

This topic is divided into four subtopics: overviews and theoretical studies of beam damage, techniques and devices to reduce beam damage, observations of beam damage with specific polymers, and studies of biological samples.

(1) General: Overviews and Theoretical Considerations

The classic overview of this field is the article by Grubb. It describes the processes and effects of radiation damage; it reviews experimental results on each of the effects of beam damage on polymers; and it considers the statistical limit placed on resolution by beam damage. Some important conclusions of the article are: heating polymer crystals always increases the rate of damage; only limited improvements result from higher accelerating voltages; and no effects are attributed to dose rate. The first two of those conclusions are considered in more depth in the earlier article by Grubb and Groves.

Other general works on beam damage include the article by Glaeser in "Introduction to Analytical Electron Microscopy", which has a good discussion of the physics involved and gives results for aromatic molecules. The two articles from "Developments in Electron Microscopy and Analysis" are also fairly general. Parkinson et al. give factors which determine a particular polymer's susceptibility to beam damage, and indicate why polyphenyls are more beam resistant than most polymers. The topics discussed by Vesely et al. include loss of material, diffraction effects, specimen charging, and contamination.

The three articles by Isaacson lean somewhat toward biological materials. "Electron Beam induced Damage..." is an important survey with helpful tables and graphs, it gives methods for reducing damage, and concludes that microanalysis is currently (1979) possible on a scale greater than 10 nm, with improvements likely in the near future. Isaacson's "Specimen Damage..." surveys the different types of experimental damage measurements (mass loss, diffraction, EELS), and notes the less-than-spectacular improvements obtained with low temperature specimens. Various expressions are explicitly given (e.g., damage dose), and theoretical resolution as a function of minimum dose is given. There is also an extensive list of references. In "The Limits...", Isaacson gives a brief general discussion about the state of affairs in the field.

Other articles which slightly emphasize biological materials include Dobb and Murray, which gives a good summary of radiation damage and contains an example of decay rate measurement. Glaeser ("Limitations...") contains quantitative measurements of radiation damage by loss of SAED intensity. Baumeister shows the chronology of radiation damage in proteins, and discusses artifacts caused by dehydration.

Ditchfield et al. compare low-dose and high-dose EELS from various polymers; an interesting hypothesis from this study is that polymer density may increase during irradiation. Boudet and Kubin derive critical dose expressions and perform an example calculation for polyethylene (e.g., maximum magnification is 54,000x).

- W. Baumeister, "Towards Higher Resolution in Biomolecular Electron Microscopy", Ultramicroscopy 9 (1982) 151.
- A. Boudet and L. P. Kubin, "The Limitations to Resolution in the Observation of Radiation-Sensitive Specimens by Electron Microscopy", Ultramicroscopy 8 (1982) 409.
- R. W. Ditchfield, D. T. Grubb and M. J. Wheelan, "Electron Energy Loss Studies of Polymers During Radiation Damage", Phil. Mag. 27 (1973) 1267.
- M. G. Dobb and R. Murray, "Towards Higher Resolution in Electron Beam Sensitive Specimens of Biological Origin", J. Microscopy 101(3) (1974) 299.
- R. M. Glaeser, "Limitations to Significant Information in Biological Electron Microscopy as a Result of Radiation Damage", J. Ultrastructure Research 36 (1971) 466.

- R. M. Glaeser, "Radiation Damage with Biological Specimens and Organic Materials", in "Introduction to Analytical Electron Microscopy", edited by J. J. Hren et al (Plenum Press, New York, 1979) p. 423.
- D. T. Grubb, "Review: Radiation Damage and Electron Microscopy of Organic Polymers", J. Mat. Sci 9 (1974) 1715.
- D. T. Grubb and G. W. Groves, "Rate of Damage of Polymer Crystals in the Electron Microscope: Dependence on Temperature and Beam Voltage", Phil. Mag. 24 (1971) 815.
- M. Isaacson, "Electron Beam Induced Damage of Organic Solids: Implications for Analytical Electron Microscopy", Ultramicroscopy 4 (1979) 193.
- M. S. Isaacson, "The Limits of Microanalytical Information as Set by Electron-Beam Damage", Proc. Ann. EMSA Meeting 41 (1983) 366.
- M. S. Isaacson, "Specimen Damage in the Electron Microscope", in "Principles and Techniques of Electron Microscopy, Volume 7: Biological Applications", edited by M. A. Hayat (Van Nostrand Reinhold, New York, 1977) p.1.
- G. M. Parkinson, M. J. Goringe, W. Jones, W. Rees, J. M. Thomas and J. O. Williams, "Electron Induced Damage in Organic Molecular Crystals: Some Observations and Theoretical Considerations", in "Developments in Electron Microscopy and Analysis", edited by J. A. Venables (Academic Press, New York, 1976) p. 315.
- D. Vesely, A. Low and M. Bevis, "The Beam Damage of Amorphous Polymers", in "Developments in Electron Microscopy and Analysis", edited by J. A. Venables Academic Press, New York, 1976) p. 333.

(2) Techniques and devices to reduce damage

Two articles discuss techniques in general. White encourages low (1000x) magnification images. Hobbs describes the damage kinetics, the process of "radiolysis", and says aromatic polymers are more stable due to electronic delocalization.

A widely studied method to reduce beam damage is cryoprotection. Knappek and Knappek et. al. discuss liquid helium sample temperatures (about a factor of 5 improvement in critical dose), consider the damage mechanisms prevalent at such temperatures, and detail superconducting lenses.

In the area of devices, Fujiyoshi et al. describe a "minimum dose system" whereby minor modifications are made to standard TEMS in order to minimize the time that the sample is in the beam during searching, focussing, and plate exposure. Thomas and Ast discuss two image intensification systems; their main advantage is to

reduce damage during focussing. Optimum magnifications and voltages are also calculated.

Lamvik and Groves gives a theoretical analysis of which can be used to determine the most efficient imaging mode (e.g., TEM or STEM, BF or DF) for a specific specimen and thickness. Misell considers contrast and signal-to-noise ratios of the various imaging modes.

Martinez et al. give experimental results on organic polymers showing very high voltages (>1 MV) can increase the specimen lifetime by a factor of 4 to 5. Three articles consider the advantages of low voltage SEM. Barth and Poole recommend a voltage of 1-3 kV, while Crewe points out the advantages of voltages in the 150 V range. Kotorman demonstrates an application to circuit analysis where the voltage is less than 1 kV.

- J. E. Barth and J. B. LePoole, "Low Voltage Electron Microscopy -How Low?", *Ultramicroscopy* 1 (1976) 387.
- A. V. Crewe, "Very Low Voltage Electron Microscopy", *Ultramicroscopy* 1 (1976) 267.
- Y. Fujiyoshi, T. Kobayashi, K. Ishizuka, N. Uyeda, Y. Ishida and Y. Harada, "A New Method for Optimal-Resolution Electron Microscopy of Radiation-Sensitive Specimens", *Ultramicroscopy* 5 (1980) 459.
- L. W. Hobbs, "Beam Sensitivity in the Electron Microscope: Strategies for Examination", *Proc. Ann. EMSA Meeting* 41 (1983) 346.
- E. Knapek, "Properties of Organic Specimens and Their Supports at 4K Under Irradiation in an Electron Microscope", *Ultramicroscopy* 10 (1982) 71.
- E. Knapek, G. Lefranc, H. G. Heide and I. Dietrich, "Electron Microscopical Results on Cryoprotection of Organic Materials Obtained with Cold Stages", *Ultramicroscopy* 10 (1982) 105.
- L. Kotorman, "Low Energy Electron Microscopy Utilized in Dynamic Circuit Analysis and Failure Detection on LSI-VLSI Internal Circuits", *IEEE Transactions on Components* 6 (1983) 527.
- M. K. Lamvik and T. Groves, "Minimization of Dose as a Criterion for the Selection of Imaging Modes in Electron Microscopy of Amorphous Specimens", *Ultramicroscopy* 2 (1976) 69.
- J. P. Martinez, D. Locatelli, J. L. Balladore and J. Trinquier, "Radiation Damage in Electron Microscopy of Organic Specimens at Very High Voltages", *Ultramicroscopy* 8 (1982) 437.

- D. L. Misell, "Conventional and Scanning Transmission Electron Microscopy: Image Contrast and Radiation Damage", J. Phys. D: Appl. Phys. 10 (1977) 1085.
- E. L. Thomas and D. G. Ast, "Image Intensification and the Electron Microscopy of Radiation Sensitive Polymers", Polymer 15 (1974) 37.
- J. R. White, "Optimum Conditions for Electron Microscopy of Radiation-Sensitive Polymer Crystals", Polymer 15 (1975) 157.

(3) Studies of specific polymers

Delgado and Hutchinson use EDS in the SEM to study chlorine loss in PVC, it is found that the elemental loss rate is an proportional to the elemental concentration, an thus an exponential decay. Read and Young determine that cross-linking is the main damage mechanism in polydiacetylene. Grubb et al. study the expansion of polyethylene crystals. Krause reports that STEM allows at least twice the dose than CTEM in his study.

Two articles are in the collection "Developments in Electron Microscopy and Analysis." Bennett et al. use multi-beam lattice-fringe images to study poly-p-phenylene terephthalamide. Thomas monitors the diffraction and dark field intensities for polyethylene.

- S. C. Bennett, M. G. Dobb, D. J. Johnson, R. Murray and B. P. Saville, "High-Resolution Studies of Electron-Beam Sensitive Polymers", in "Developments in Electron Microscopy and Analysis", edited by J. A. Venables (Academic Press, New York, 1976) p. 329.
- L. A. Delgado and T. E. Hutchinson, "Elemental Loss During Electron Beam Irradiation", Ultramicroscopy 4 (1979) 163.
- D. T. Grubb, A. Keller and G. W. Groves, "Origin of Contrast Effects in the Electron Microscopy of Polymers", J. Mat. Sci. 7 (1972) 131.
- S. J. Krause, "Specification of Damage Criteria in Electron Microscopy of Polyethylene Film and Crystals", Proc. Ann. EMSA Meeting 40 (1982) 676.
- R. T. Read and R. J. Young, "Radiation Damage and High Resolution Electron Microscopy of Polydiacetylene Crystals", J. Mat. Sci. 19 (1984) 327.
- E. L. Thomas, "Electron Microscopy of Radiation Sensitive Polyethylene Crystals", in "Developments in Electron Microscopy and Analysis", edited by J. A. Venables (Academic Press, New York, 1976) p. 293.

(4) Studies of biological samples

Chiu and Jeng discuss the merits of different ways to measure damage from diffraction intensities. Reimer and Spruth give experimental results for the fading of diffraction for 10 organic compounds as a function of temperature, and fit their results to theory. Salih and Cosslett examine the cold stage beam damage of three organic molecules. Glaeser and Hobbs observe an increase of damage to their sample at low temperature and attribute it to staining. Isaacson et al. study the radiation damage of 2 biomolecules with EELS; it is found that some components are readily lost while others exhibit a "latent dose" effect.

W. Chiu and T. W. Jeng, "Quantitative Assessment of Radiation Damage in Protein Crystals", Proc. Ann. EMSA Meeting 41 (1983) 356.

R. M. Glaeser and L. W. Hobbs, "Radiation Damage in Stained Catalase at Low Temperature", J. Microscopy 103,2 (1975) 209.

M. Isaacson, M. L. Collins and M. Listvan, "Electron Beam Damage of Biomolecules Assessed by Energy Loss Spectroscopy", in "Electron Microscopy 1978, Volume III: State of the Art Symposia (Proceedings of the Ninth International Congress on Electron Microscopy)", edited by J. Sturgess (Microscopical Society of Canada, Toronto, 1978) p. 61.

L. Reimer and J. Spruth, "Interpretation of the Fading of Diffraction Patterns from Organic Substances Irradiated with 100 KeV Electrons at 10-300K", Ultramicroscopy 10 (1982) 199.

S. M. Salih and V. E. Cosslett, "Studies on Beam Sensitive Substances", in "Developments in Electron Microscopy and Analysis", edited by J. A. Venables (Academic Press, New York, 1976) p. 311.

APPENDIX B

EFFECTS OF BEAM DAMAGE

Beam damage is an important consideration when investigating polymers by electron microscopy. Beam damage can affect the results of both conventional and analytical electron microscopy techniques. In this appendix, the rate of beam damage of PBT and ABPBI is found by the decay of diffraction intensities. The changes in EELS and EDS data with dose are presented and discussed.

Beam damage of polymers progresses in definite stages. Among the important changes that occur are loss of crystallinity, changes in bonding, loss of mass, and large-scale morphological changes (image artifacts). Accurate data is obtained only before any significant changes take place, thus limiting the total electron dose to an area of the sample. Therefore, it is important to monitor the effects of beam damage to ensure the integrity of the results. Fortunately, aromatic polymers are generally much more resistant to beam damage than other types of polymers (assumed to be due to delocalization of electrons), and PBT and ABPBI are no exception.

Since a change in crystallinity is usually the first effect of beam damage to be detected, a good indication of a polymer's susceptibility can be obtained from the changes in its diffraction pattern intensity. Figure B-1 is a best-fit plot of diffracted intensities for various PBT and ABPBI reflections versus electron dose at room temperature, based on a study by S. Kumar, S. J. Krause and W. W. Adams (Proc. Ann. EMSA Meeting 43 (1985), to be published). Diffraction intensity $i(D)$ follows an exponential decay given by $i(D) = C \exp(-D/D^*)$, where C is a constant, D is the electron dose, and D^* is the dose at which the diffracted intensity is $1/e$ of its original value. For ABPBI, D^* is about $0.6 \text{ coulombs/cm}^2$; for PBT, D^* is between 1 and 2 coulombs/cm^2 . These values are two and three orders of magnitude higher than the value of D^* for polyethylene, demonstrating the relative beam resistance of PBT and ABPBI.

In order to determine the specific effects of beam damage on AEM, both EDS and EELS spectra were taken after various amounts of irradiation of PBT and ABPBI. Figure B-2 shows two EDS spectra for PBT. The first spectrum Figure B2a was taken after a few seconds of irradiation—near the minimum dose to obtain a statistically meaningful spectrum. Then after several minutes of irradiation, a second spectrum

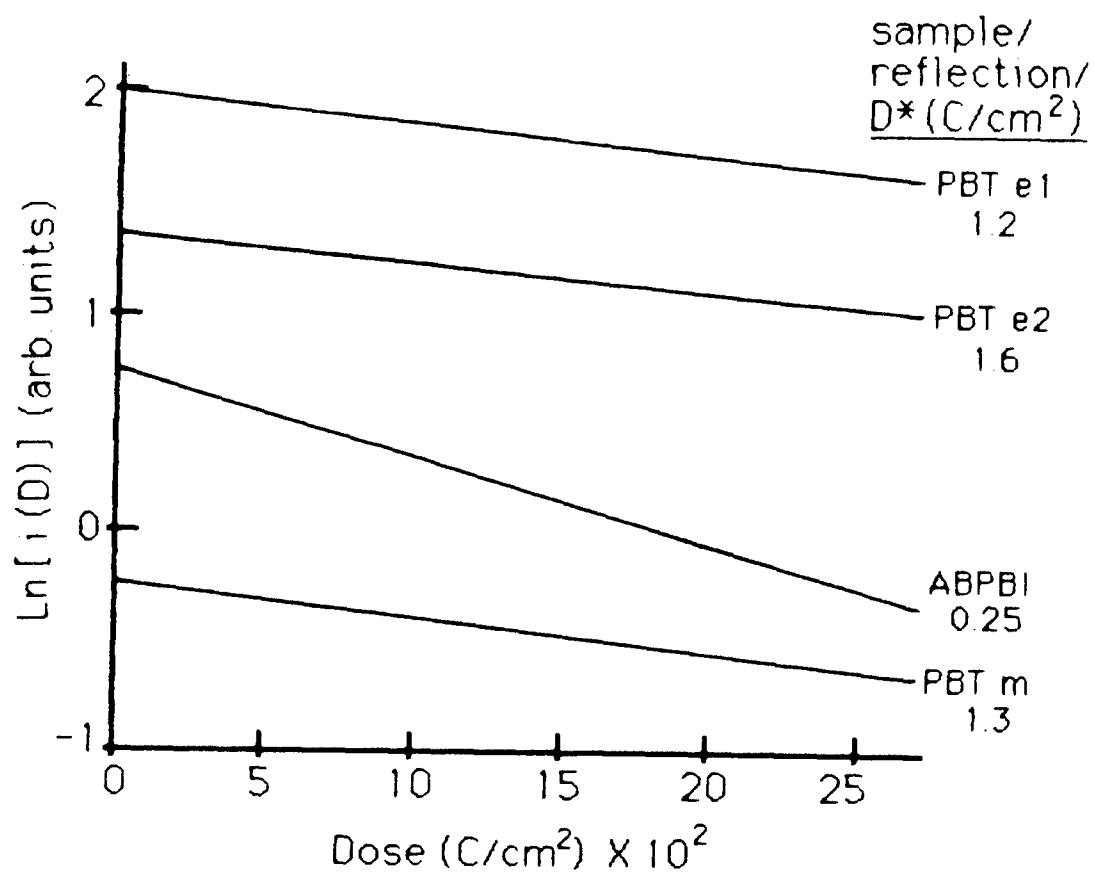


Figure B-1 Diffraction Intensity vs. Electron Dose for Various SAED Reflections of PBT and ABPBI

was obtained (Figure B2b). The copper peaks are background, but their intensities can be used as a reference. The sulfur peak is essentially the same, so no significant loss of sulfur occurred during the irradiation period. This indicates that EDS can be used validly with PBT. Figure B3 shows the corresponding data for ABPBI. Here, the sulfur is due to a processing solvent, but again there is no mass loss evident for ABPBI.

Figure B4 represents a similar experiment involving the EELS spectra of PBT. Although the sample used here is too thick for the sulfur edge to be apparent, the carbon edge is visible. There are no significant changes between the first spectrum Figure B4a and the spectrum obtained after several minutes of irradiation (Figure B4b). Figure B5 shows the progression of the EELS spectra for ABPBI. Although there are no changes apparent from the first spectrum (Figure B5a) to the spectrum obtained after several minutes of irradiation (Figure B5b), some changes occur after heavy irradiation (Figure B5c). The carbon edge has become more prominent, an indication of mass loss since this reduces the multiple scattering which increases background. The observation of this with ABPBI and not PBT is consistent with the above result of a higher value of D^* for PBT.

Overall, neither PBT nor ABPBI exhibit any significant changes in either their EDS or EELS spectra with doses necessary for the acquisition of the spectra, supporting the validity of AEM of these polymers.

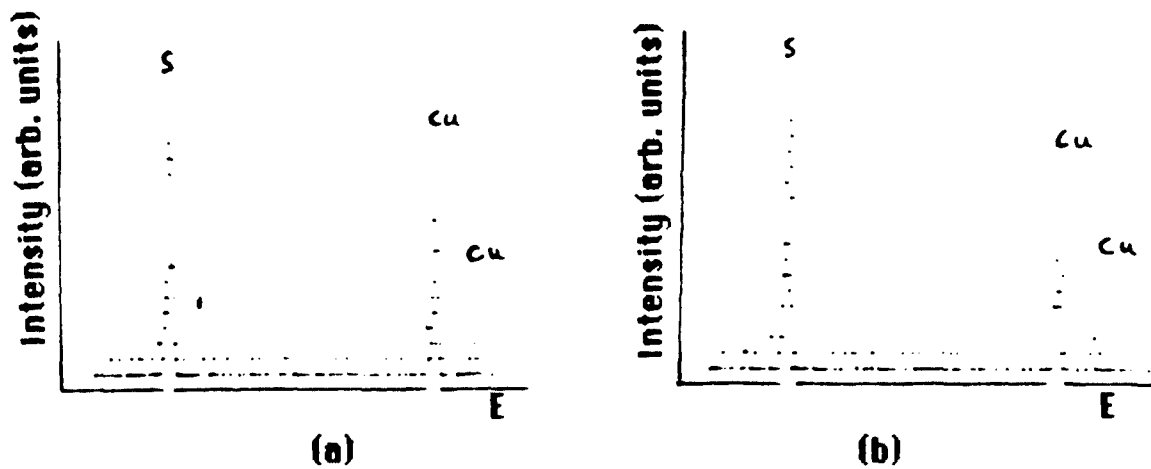


Figure B-2 Energy Dispersive X-ray Spectra for PBT

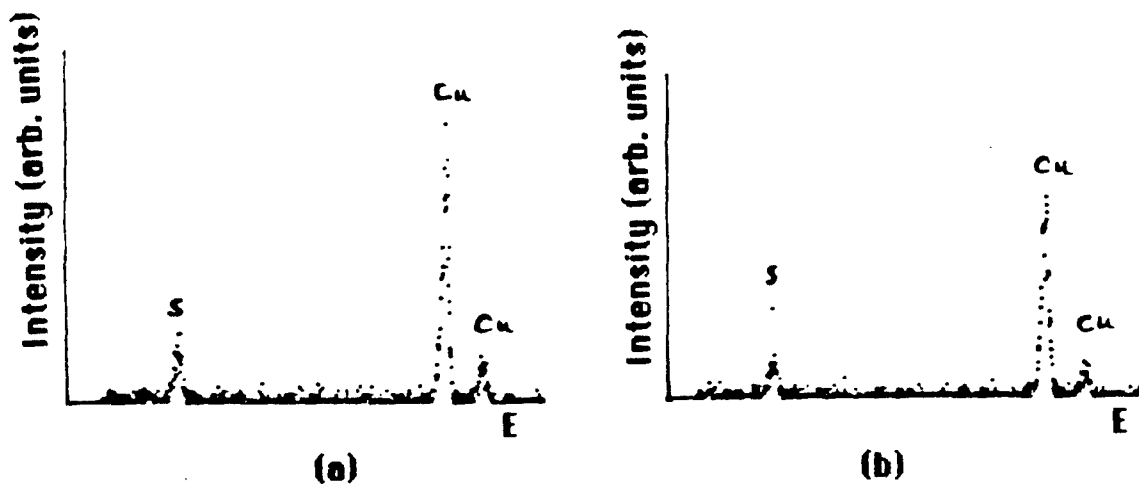


Figure B-3 Energy Dispersive X-ray Spectra for ABPBI

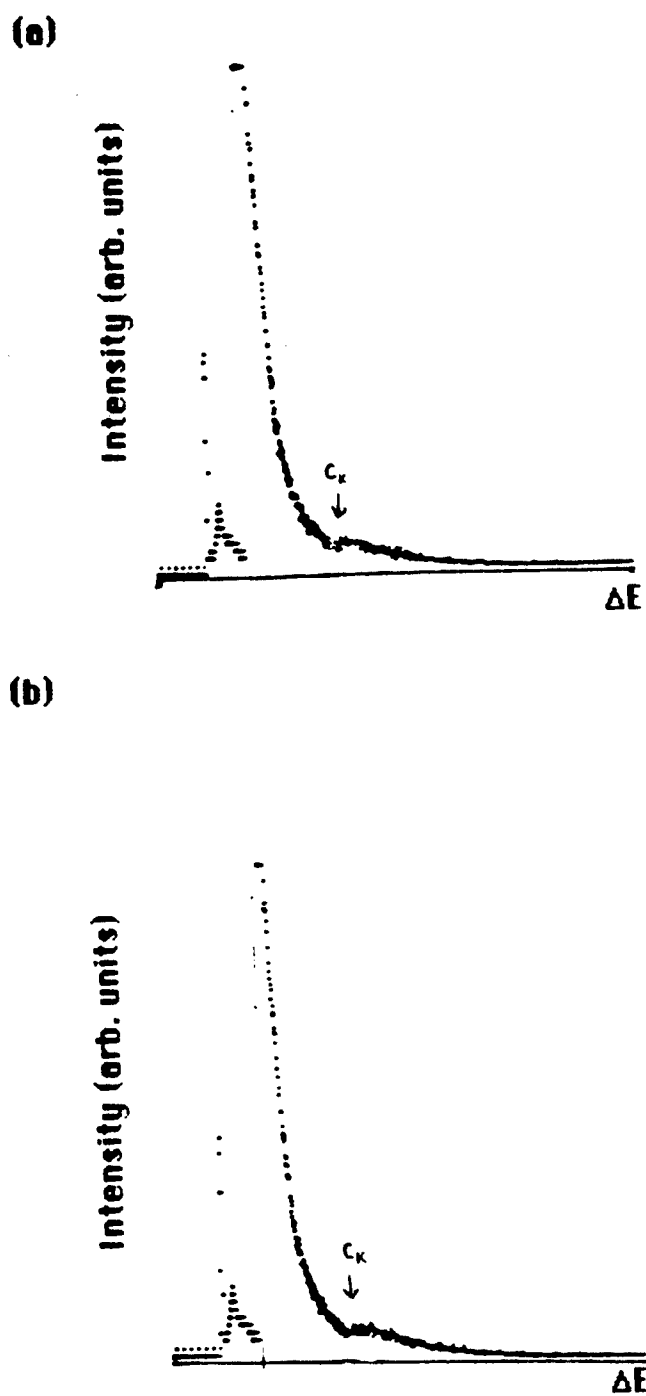


Figure B-4 Electron Energy Loss Spectra for PBT

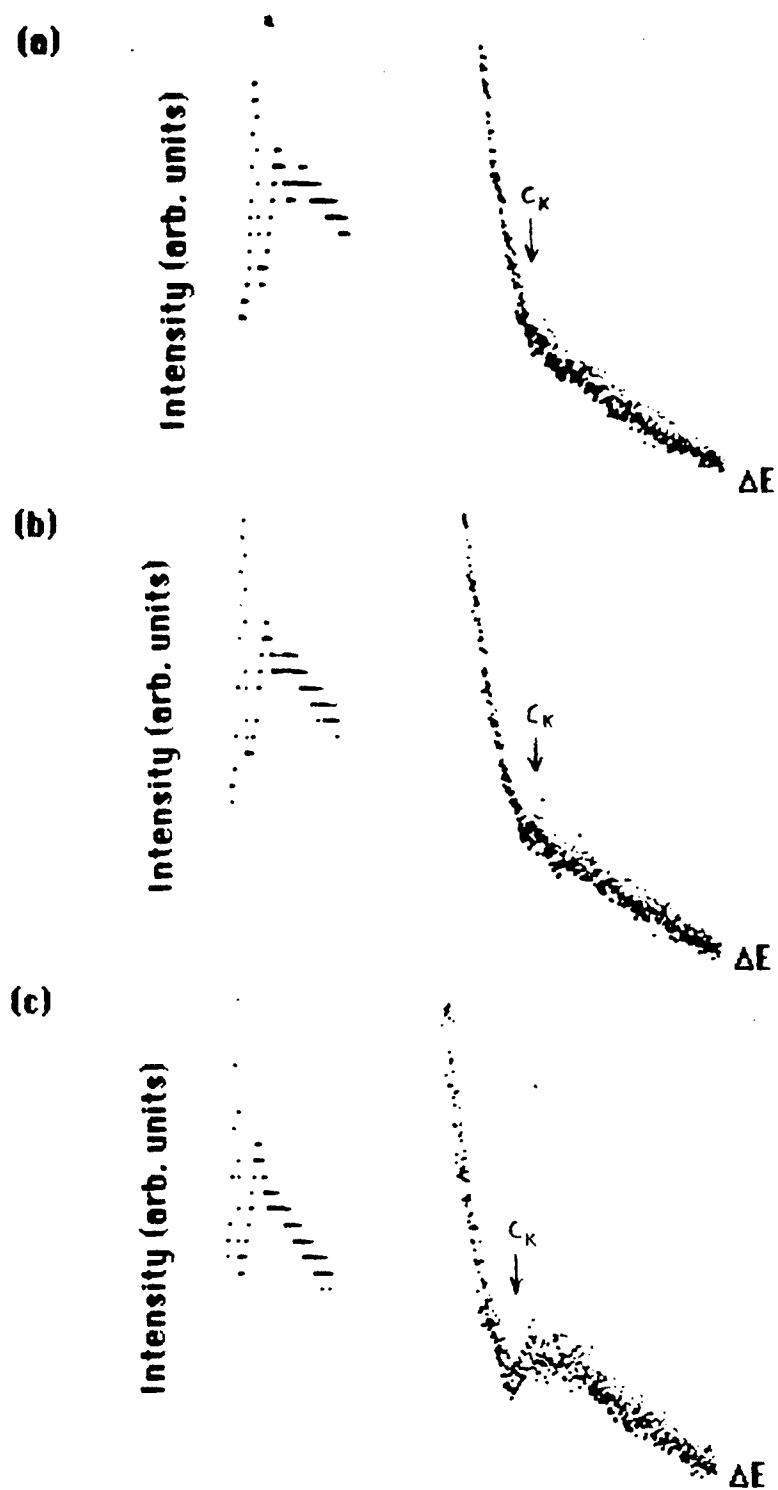


Figure B-5 Electron Energy Loss Spectra for ABPBI

APPENDIX C

ANALYTICAL ELECTRON MICROSCOPY BACKGROUND

The various techniques of analytical electron microscopy (AEM) can be used to study certain types of electron-sample interactions which can give both chemical and structural information on a scale finer than one micron. AEM techniques have evolved along with the scanning transmission electron microscope (STEM). In TEM, the sample is illuminated by a "flood-beam" of electrons. The smallest beam size is usually a few microns. In STEM, a fine probe, as small as 1 to 10 nm, is scanned over an area of a sample (analogous to a TV raster) while detectors collect signals from individual points on the sample. The detector outputs modulate the intensity of a scanning beam in a cathode ray tube and are synchronized with the scanning beam on the sample in order to display a serially collected image of the desired information. By locking the beam at a fixed point of interest on the sample, information can also be obtained from very small areas.

It is important to note that in any of the electron microscopy techniques discussed in this report, electrons are impinging on the sample. The difference between TEM imaging and diffraction techniques and AEM techniques is that there are numerous signals available from individual points in the sample in AEM. Thus, the consideration about beam damage, as discussed earlier for TEM, apply to AEM as well.

Since the mid-1970s, instruments which combine TEM, STEM, and AEM have been readily available commercially. The analytical accessories are usually operable in either TEM or STEM modes, but STEM is generally preferred because of easier data manipulation and control of electron dose. In the past few years, SEMs with similar analytical capabilities have also been developed. Both of these types of microscopes, STEM/AEM and SEM, were utilized for the microanalysis in this report.

The principles of energy dispersive x-ray analysis (EDS) are as follows. As the electron beam passes through the sample, energy is imparted to inner shell electrons of the atoms in the sample. When electrons from higher energy levels drop back to the originally occupied inner shell energy levels, x-rays are emitted. Since each element has a unique set of energy levels, the energy of the emitted x-rays can be used to determine the elements present in the sample. Moderately accurate quantitative compositional analysis is also possible with many samples.

The energies of the emitted x-rays are measured with a solid state detector, usually lithium-doped silicon known as Si(Li), located above and to the side of the sample in the electron microscope. The sample is tilted toward, and is located as close as possible to, the detector in order to maximize detection efficiency. As x-rays enter the detector, electron-hole pairs are created, the number of which depends on the energy of the x-ray. As x-rays are collected over a period of time, data about the number of x-ray counts versus x-ray energy is stored in a multichannel analyzer, resulting in a spectrum of counts versus energy.

An optional mode of operation in EDS is x-ray elemental mapping. By specifying a limited energy range which is characteristic of a specific element (an energy "window"), the system can semi-quantitatively register the concentration of that element at each point as the electron beam is scanned across a sample area. The resultant data pattern is known as a x-ray elemental map. A superposition of this data upon an image of the same area can be useful for comparing the distribution of elements with the sample morphology.

The basic principles of electron energy loss spectroscopy are as follows. Some electrons lose a small amount of energy ($<1\%$) as they inelastically interact with atoms while passing through the sample. These electrons experience a very slight deflection and continue through the microscope column along with the unscattered electrons. These electrons can be focussed into a magnetic spectrometer which separates the electrons into a spectrum according to their energies and, therefore, their energy loss. This is analogous to a prism separating light into a spectrum. An additional dc offset field is applied which causes the spectrum of energies to be sequentially scanned over a slit, and a photomultiplier tube converts the number of electrons at a certain energy loss into a signal which goes to a multichannel analyzer. Thus, a graph of counts or intensity versus energy loss is obtained. This is an electron energy loss spectrum.

The EELS spectrum consists of three general regions: the zero-loss peak, the low loss region, and the higher-loss region. The zero-loss peak consists basically of unscattered electrons and is used for the reference energy of the spectrum. The low-loss region extends out to energy losses of about 50 eV. For polymers, the region contains information about molecular orbitals and bonding, although detailed interpretations are difficult. The primary features of the higher-loss region are

peaks which occur at the "ionization edges". Each of these peaks represents the energy lost in removing electrons from a particular atomic shell (K, L, etc.). Since each element has unique ionization energies, this part of the spectrum can be used to identify the elements which are present in a sample, in a manner analogous to x-ray microanalysis. The sulfur and nitrogen ionization edges were useful here to distinguish between PBT and ABPBI.

The technique of microdiffraction is a standard feature on STEM instruments. In microdiffraction, a small beam of electron probes the crystalline structure in an area of the sample typically 20 nm in diameter. The resultant diffraction pattern provides the same type of information as SAED (size, shape, and orientation of crystallites), but from a much smaller area.

THIS DOCUMENT CONTAINED
BLANK PAGES THAT HAVE
BEEN DELETED